Role of isolated acid sites and influence of pore diameter in the low-temperature dehydration of ethanol

Potter, Matthew E; Cholerton, Mary E.; Kezina, Julija; Bounds, Richard; Carravetta, Marina; Manzoli, Maela; Gianotti, Enrica; Lefenfeld, Michael; Raja, Robert. Role of isolated acid sites and influence of pore diameter in the low-temperature dehydration of ethanol. ACS CATALYSIS. 4 (11) pp: 4161-4169.
DOI: 10.1021/cs501092b

The Role of Isolated Acid Sites and Influence of Pore Diameter in the Low-Temperature Dehydration of Ethanol

Matthew E. Potter,[†]* Mary E. Cholerton,[†] Julija Kezina,[†] Richard Bounds,[†] Marina Carravetta,[†] Maela Manzoli,[‡] Enrica Gianotti,[ζ] Michael Lefenfeld,[ϕ] and Robert Raja[†]*

[†]*School of Chemistry, University of Southampton, University Road, Southampton, SO17 1BJ, United Kingdom*

[‡]*Department of Chemistry & NIS-Interdepartmental Centre, University of Turin, Via P. Giuria, 10125, Torino, Italy*

[ζ]*Dipartimento di Scienze e Innovazione Tecnologica, Centro Interdisciplinare Nano-SiSTeMI, Università del Piemonte Orientale, Via T. Michel 11, 15100, Alessandria, Italy*

[ϕ]*SiGNa Chemistry Inc, 845 Third Avenue, Suite 623, New York City, New York 10022, United States*

ABSTRACT: Silicoaluminophosphates, SAPO-5 and SAPO-34, differ not just in their pore-diameters and structural topology, but in their preferred mechanism of silicon substitution into the framework, which subsequently influences the nature of the acid sites for solid-acid catalyzed transformations. This study combines ^{29}Si NMR, FTIR and DFT calculations for probing the nature of the isolated acid sites, thereby affording structure-property correlations, in the low-temperature catalytic dehydration of ethanol to ethylene.

KEYWORDS: Ethanol dehydration, SAPO, Solid-acid, ^{29}Si NMR, single-site, synergy, structure-activity relationships

1. INTRODUCTION

Decreasing reserves of fossil fuels coupled with growing environmental concerns have increased demands from the plastics and polymer industry[1] for a source of ethylene prepared via an affordable and benign process. Currently a significant quantity of the world's ethylene is dependent on cracking hydrocarbon liquids;[2] however the declining interest in using ethanol as a motor fuel has resulted in a vast surplus of an alternative, sustainable feedstock, bio-ethanol.[3] Conventionally the dehydration of ethanol to ethylene was performed using caustic mineral acids, the aggressive nature of which results in the co-production of inorganic waste. These effects can be elegantly negated through the use of a recyclable and recoverable solid-acid catalysts.

The challenge of generating ethylene from ethanol using solid acid catalysts has been approached using a wide-range of materials such as metal-oxides,[4] heteropolyacids[5] and porous solids.[6] Porous solids such as zeolites and their related zeotype analogues, aluminophosphates (AlPOs) are known for their ability to combine catalytically active, isolated metal sites with a variety of microporous frameworks.[7] Silicon is the most common dopant in AlPO materials, as the similarity in size between silicon and the framework atoms aids isomorphous substitution. However, both the size and charge of the Si^{4+} dopant ion lie between that of the Al^{3+} and P^{5+} framework ions, resulting in a range of possible substitution mechanisms and consequently a variety of silicon sites may be generated. One such mechanism is known as type II substitution; whereby silicon (Si^{IV}) substitutes exclusively for phosphorus (P^{V}). This substitution causes a charge imbalance within the neutral AlPO framework which results in the formation of an isolated, catalytically active, Brønsted acid site. Alternatively, a type III substitution mechanism can also occur whereby two silicon (Si^{IV}) ions substitute an adjacent aluminum (Al^{III}) and phosphorus pair (P^{V}). In this situation the charges are equal and as such no protons are required for charge-compensation[8] (See Figure S1). The latter leads to the formation of silicon clusters or 'islands' whereby multiple silicon environments and acid sites are generated, and can be observed and rationalized using a range of physico-chemical spectroscopic characterization techniques.

Much of the original interest in zeotype materials originated from the ability to selectively combine specific framework architectures with a well-defined catalytically active site. Through the use of targeted synthetic strategies it has been demonstrated that AlPOs can be designed for a range of industrially-relevant transformations such as catalytic cracking,[9] alkylation and isomerization reactions.[10] In this study we employ a multi-technique characterization approach, to simultaneously explore the influence of framework selection and silicon loading on the nature and precise location of Brønsted acid sites in silicon-substituted AlPOs.[11] This in-depth characterization investigation is subsequently complimented by theoretical findings, linking the specific nature of the acid sites observed to their catalytic efficacy. The catalytic potential of such species is then explored as they have proved effective in acid-catalyzed dehydration reactions, with an aim to further development of a low-temperature process for the dehydration of ethanol to ethylene.

2. EXPERIMENTAL SECTION

2.1.Materials

SAPO-34 and SAPO-5 materials were prepared using reported literature procedures.[12-14] Key ingredients and synthesis conditions are reported in Tables 1 and S1.

2.2. Characterization

^{29}Si solid-state NMR measurements were performed on a Chemagnetics Infinity console with a Bruker 9.4 T magnet and a 4 mm double-resonance APEX probe. The resonance frequencies at this field strength were 79.6 (^{29}Si) and 400.8 MHz (^{1}H). For all samples, approximately 80 mg of the freshly calcined material was transferred to a thin-wall zirconium oxide rotor, and spun at 8kHz using nitrogen gas for bearing and drive. The spectra were acquired using ramped cross polarization with a contact time of 8 and 4ms for SAPO-5 and -34, respectively, with a 5% ramp and SPINAL64 decoupling with a nutation frequency of 63 kHz. The spectra are the results of 25000 and 15000 scans for SAPO-5 and SAPO-

34, respectively, with 4 s pulse delay. The ^{29}Si chemical shift scale was referenced with respect to silicon rubber (–22.3 ppm).[15] All spectra were recorded at room temperature under nitrogen. The data was processed using MatNMR.[16]

FTIR spectra of self-supporting wafers of the samples (ca. 5 mg cm^{-2}) were recorded with a Bruker IFS22 spectrometer at a resolution of 4 cm^{-1}. All samples were re-calcined at 823 K in oxygen to clean the surface from pre-adsorbed species before the FTIR experiments. CO (initial pressure = 30 Torr) was adsorbed at 80 K on the calcined samples, using specially designed cells, which were permanently connected to a vacuum line (ultimate pressure $<10^{-5}$ Torr) to perform *in situ* adsorption-desorption measurements. FTIR spectra were normalized with respect to the pellet thickness and are reported in difference mode by subtracting the spectrum of the sample in vacuo to the spectrum of the CO adsorbed molecules. Multi-peaks fit was performed by employing ORIGIN 6.1 Scientific Graphing and Analysis Software. Lorentzian functions were used and R^2 values above 0.99173 were obtained for all curve fittings.

2.3.Catalysis

The catalytic reactor (quartz) was packed with a thin layer of 1 mm glass beads on top of the frit followed by the catalyst in pellet form up to a height of 40 mm (approximately 0.3 g), which was then topped with a 70 mm layer of glass beads to minimize the dead volume. A solution of 10 g heptane in ethanol was prepared in a 100 mL volumetric flask; this solution was pumped through the system to ensure that all dead volume was occupied with the solution. The helium carrier gas was started (50 mL min^{-1}) and the reactor was heated to the desired reaction temperature. The syringe pump was loaded (WHSV = 4.38 h^{-1}) and the system allowed to equilibrate for 1 hr prior to a gas chromatography sample (0.25 mL) being taken. Similarly samples were taken after 3 h, and no significant change was observed. Product analysis was carried out using a Perkin Elmer GC employing an Elite 5 column (Crossbond 5% diphenyl- 95% dimethyl polysiloxane, 30 m, 0.25 mm id) using an isothermal method program employing heptane as the internal standard.

2.4.Computational data

Computational *ab initio* calculations were performed on the University of Southampton Iridis3 super-cluster with the CRYSTAL09 periodic DFT code[17] using the B3LYP hybrid-exchange functional.[18-21] All atoms were described using a double valence plus polarization basis set. All basis sets employed were taken from the online library for the CRYSTAL code.[22] The AFI structure was computed by initially modelling a unit cell containing 72 atoms (12 aluminium, 12 phosphorus and 48 oxygen atoms). Similarly the CHA structure was computed by initially modelling a unit cell containing 108 atoms (18 aluminium, 18 phosphorus and 72 oxygen atoms). In the case of a charge imbalance (Si^{4+} substituting P^{5+}) a proton was attached to an oxygen molecule adjacent to the divalent or tetravalent substituent. No geometric constraints were employed in the optimization procedure.

The energy of substitution (Δ_{Sub}) was calculated for the 3 sites by using equations 1-3.

(1) $\Delta_{sub,1} = E[H_1Si_1Al_xP_{x-1}O_{4x}] + E[P(H_2O)_5(OH)^{4+}] - E[Al_xP_xO_{4x}] - E[Si(H_2O)_6^{4+}]$

(2) $\Delta_{sub,2} = E[Si_2Al_{x-1}P_{x-1}O_{4x}] + E[P(H_2O)_6^{5+}] + E[Al(H_2O)_6^{3+}] - E[Al_xP_xO_{4x}] - 2E[Si(H_2O)_6^{4+}]$

(3) $\Delta_{sub,5} = E[H_3Si_5Al_{x-1}P_{x-4}O_{4x}] + E[P(H_2O)_6^{5+}] + E[Al(H_2O)_6^{3+}] + 3E[P(H_2O)_5(OH)^{4+}] - E[Al_xP_xO_{4x}] - 5E[Si(H_2O)_6^{4+}]$

It is to be noted that due to the use of semi-stable octahedral-coordinated ions it is not possible to draw comparisons between energy values of different sites; only the same sites in different frameworks are taken into consideration.

Binding studies were also performed with NH3 and ethanol on the specific sites evidenced by ^{29}Si NMR, to gain an insight into the acidic nature of the specific active sites and the mechanistic implications. The following equation was used to quantify the degree of interaction with the probe molecules:

(4) $\Delta_{Binding} = E[Probe + SAPO] - E[Probe] - E[SAPO]$

3. RESULTS AND DISCUSSIONS

SAPO-5(1.38) and SAPO-34(2.66) were successfully synthesized according to the procedures described in the Supporting Information (Tables 1 & S1). Powder X-ray diffraction (Figure S2 & S3) confirmed the structural integrity of the materials, with the unit cell parameters (Table S2) showing only subtle variations from the ideal values owing to the framework incorporation of relatively small quantities of silicon, as evidenced through ICP (Table 1). The morphology of the particles was examined using scanning electron microscopy (Figure S5 & S6), while BET measurements confirmed the porous nature of the materials (Table S3). The initial characterization of both catalysts revealed structural and physicochemical attributes, such as surface area and particle size (Tables S3 and S4) were in good agreement with reported literature values and each other (where appropriate).[23,24] Given the disparity in silicon content between the phase-pure SAPO-5(1.38) and SAPO-34(2.66) samples, the gel compositions were modified such that both samples would possess comparable quantities of silicon, thus forming SAPO-5(1.80) and SAPO-34(1.82). While the silicon loadings were indeed in good agreement, (Table 1) the minor phase impurities were present, with both powder XRD patterns showing signs of secondary phases (Figure S4). This observation is a direct consequence of our employment of analogous synthetic tools

Table 1: Gel compositions and ICP values of SAPO catalysts

Catalyst	Molar gel composition	Al/wt%	P/wt%	Si/wt%
SAPO-5(1.38)	1.0Al:1.0P:0.2Si:50TEA:18H_2O	18.93	21.16	1.38
SAPO-5(1.80)	1.0Al:1.0P:0.4Si:50TEA:18H_2O	21.07	22.61	1.80
SAPO-34(1.82)	1.0Al:1.0P:0.08Si:1.0TEAOH:50H_2O	24.87	17.97	1.82
SAPO-34(2.66)	1.0Al:1.0P:0.15Si:1.0TEAOH:50H_2O	17.19	16.74	2.66

to form these catalytic species. As such the synthesis procedures for the two SAPO-34 (and SAPO-5) samples varied only by the silicon gel ratios used in the synthesis. This finding emphasizes the importance of using the optimal gel compositions in synthetic protocols, thus even subtle modifications of a single parameter can expedite the formation of alternative phases, and thereby influence the nature and strength of the resulting active (acid) centers.

The acid strength of the Brønsted sites in SAPO-34 (2.66 and 1.82) and SAPO-5 (1.38 and 1.80) catalysts has been monitored by using FTIR spectroscopy employing CO as a molecular probe. In particular, the shift of the bands of the hydroxyl groups ($\Delta\nu_{OH}$) by the adsorption of small molecules (N_2, CO, etc.), which act as weak bases forming OH···CO hydrogen-bonded adducts with the Brønsted sites, has been used to estimate the acidity of Brønsted sites.[25,26]

SAPO-34 catalysts, in the OH stretching range (Figure 1A), display a feature at 3678 cm^{-1}, due to P-OH defects, and two intense bands with maxima at around 3630 and 3600 cm^{-1}, (labeled as OH_A and OH_C) that have been assigned to Al(OH)Si Brønsted acid sites with different acid strengths in O4 and O2 structural configurations in the CHA framework, respectively.[27-29] The presence of a third component at 3610 cm^{-1}, labeled as OH_B, (Figure 1A) although weak, was clearly evident, and it has been proposed[27,30] that this component, characterized by a strong acid character comparable to that found in the aluminosilicate H-SSZ-13 homologue,[29,30] cannot be simply interpreted in terms of structural configurations (as proposed for the OH_A and OH_C) but, is more attributable to the local environment in the immediate vicinity of the active site.[31-34]

In contrast, the SAPO-5 catalysts exhibit two well separated bands at 3630 cm^{-1}, labeled as OH_A' and 3513 cm^{-1}, labeled as OH_B' (Figure 1B). Both bands are associated with the Al(OH)Si Brønsted acid sites in different positions inside the AFI framework. The high frequency band is due to sites located in the 12-ring channels, whilst the band at 3513 cm^{-1} can be attributed to bridging OH located in the 6-ring channels.[35-37] No defects due to Si-OH (3745 cm^{-1}) or P-OH (3678 cm^{-1}) sites are present in the SAPO-5 catalyst.

By comparing the intensity and the integrated area (A_0) of the bands due to the Brønsted acid sites (Fig.1A and Table 2) for SAPO-34 catalysts we have observed that the SAPO-34 (2.66) has an higher fraction of Brønsted sites with respect the SAPO-34 (1.82), which is consistent with the higher Si content. On the contrary, SAPO-5 (1.38) has a higher fraction of Brønsted sites (Fig.1B and Table 2) when compared to the higher Si content SAPO-5 (1.80) catalyst, probably due to the different Si substitution mechanism in the SAPO-5 framework (Figure S1), that results in the formation of extra-framework species and silicon islands.

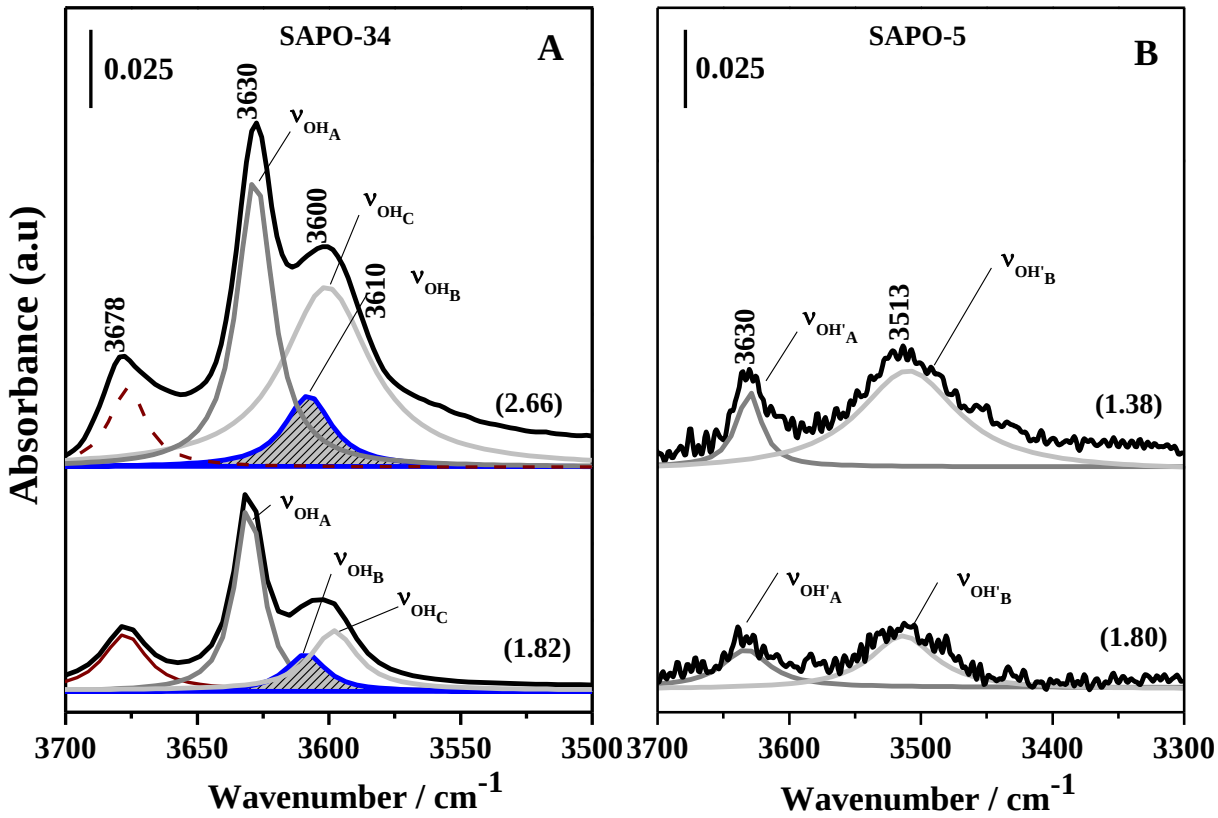

Figure 1 FTIR spectra in the OH stretching region of calcined SAPO-34 (2.66) and SAPO-34 (1.82) catalysts (**A**), and SAPO-5 (1.38) and SAPO-5 (1.80) catalysts (**B**). The different OH components are evidenced by the curve fitting – see Table 2.

TABLE 2: Position of the Maxima, Full-Width at Half Maximum (fwhm), and Integrated Area (A0) of the Peaks Obtained by Curve Fitting of the □OH spectra of SAPO-34 and SAPO-5 samples reported in Fig.1.

	SAPO-34 (2.66)			SAPO-34 (1.82)		
	ν_{OH} (cm^{-1})	*fwhm* (cm^{-1})	*A0*	$\nu_{OH...}$ (cm^{-1})	*fwhm* (cm^{-1})	*A0*
OH_A	**3630**	**16.54**	**2.46**	**3630**	**12.71**	**1.23**
OH_B	**3610**	**20.53**	**0.69**	**3608**	**18.07**	**0.35**
OH_C	**3600**	**26.84**	**1.89**	**3600**	**21.24**	**0.65**
	SAPO-5 (1.38)			SAPO-5 (1.80)		
	ν_{OH} (cm^{-1})	*fwhm* (cm^{-1})	*A0*	$\nu_{OH...}$ (cm^{-1})	*fwhm* (cm^{-1})	*A0*
OH_A'	**3630**	**22.50**	**0.87**	**3633**	**43.24**	**0.83**
OH_B'	**3513**	**91.65**	**4.73**	**3513**	**59.22**	**1.63**

The acid strength of the Brønsted sites was elucidated by adsorbing CO at 80 K on all SAPO-34 and SAPO-5 samples (Figure S7 and Table 3). The SAPO-34 and SAPO-5 catalysts displayed an analogous behavior upon CO adsorption at 80K despite the different Si content, and the results for the SAPO-34 (2.66) and SAPO-5 (1.38) catalysts, which possess the higher fraction of Brønsted acid sites (Fig.1) are rationalized below. Upon CO interaction at low temperature with SAPO-34 and SAPO-5, the bands due to Si(OH)Al Brønsted acid sites present in the 3630-3600 cm^{-1} range are shifted downwards, forming a broad and intense absorption in the 3500-3200 cm^{-1} interval due to the OH···CO H-bonded adducts. Only the band at 3513 cm^{-1}, attributed to Si(OH)Al located in the 6-ring channels of SAPO-5 is not shifted and remains unperturbed, implying that these Brønsted acid sites are not accessible, even to small molecules such as CO and therefore do not contribute to the acidity in the SAPO-5 catalyst. In Table 3 the position of the maxima of the Brønsted acid sites before and after CO perturbation and the resulting

$\Delta\nu_{OH}$ shifts for both SAPO-34 and SAPO-5 are reported. The position of the OH_A, OH_B and OH_C····CO adducts in SAPO-34 was obtained by a multi peak curve-fitting approach (Figure 3). Moreover, the shoulder at 3540 cm^{-1} visible upon CO adsorption (Figure 2) is due to CO interacting with a fraction of P-OH defects; and is consistent with the observation of the P-OH (3678 cm^{-1}) feature that does not completely disappear upon CO interaction.[38]

The $\Delta\nu_{OH}$ is a measure of the acid strength: the stronger the Brønsted acidity, the larger is the $\Delta\nu_{OH.}$ The $\Delta\nu_{OH}$ arising from the band due to OH_B sites in SAPO-34 is very large, with respect to the reported values for Brønsted acid sites in SAPO structures; which are normally less acidic than those of analogous aluminosilicate structures, such as H-SSZ-13 ($\Delta\nu_{OH}$ = 316 cm^{-1}),[29,31] where Si(OH)Al Brønsted sites are formed by the introduction of Al sites into the silicalite framework. It has been hypothesized that these types of strong Brønsted acid sites that can be influenced by a particular type of substitution mechanism (Figure S1)[39,40] in SAPOs, resemble and mimic analogous sites in aluminosilicates.[27,30,34] By comparing the $\Delta\nu_{OH}$ values for the signals present in SAPO-5 and SAPO-34 it is clear that the overall acidity generated by the Brønsted sites in SAPO-34 is much stronger than that of the SAPO-5 species. This is exemplified by the fact that the OH_A signal is marginally stronger than that of the OH_A', but more particularly to the presence of the highly acidic OH_B species as well as to the additional presence of OH_C groups in the SAPO-34 catalyst. It is highly likely that the advantageous combination of the OH_A, OH_B and OH_C sites in the SAPO-34 catalyst could be directly responsible in modulating the degree of acidity and play a pivotal role in enhancing the catalytic activity, when compared to its SAPO-5 counterpart.

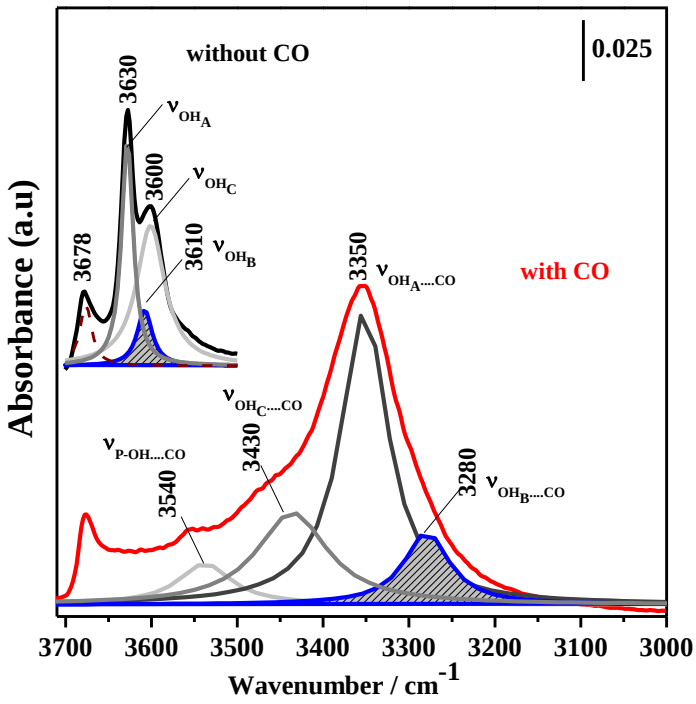

Figure 2 FTIR spectra in the OH stretching region of calcined SAPO-34 (2.66) in vacuo (black curve) and upon adsorption of CO (red curve) at 80 K. Spectra of the unperturbed hydroxyls with OH_A, OH_B and OH_C components (grey and blue lines) and of OH$^{\cdots}$CO adducts are obtained by a curve fitting procedure. A good fit of the OH and OH$^{\cdots}$CO adduct bands can only be obtained using three components.

TABLE 3: Position of maxima of OH Brønsted sites and their shifts ($\Delta\nu_{OH}$) upon CO adsorption at 80K on SAPO-34 and SAPO-5.

Catalysts		ν_{OH} (cm^{-1})	$\nu_{OH\ldots CO}$ (cm^{-1})	$\Delta\nu_{OH}$ (cm^{-1})
SAPO-34	OH_A	**3630**	**3350**	**280**
	OH_B	**3610**	**3280**	**330**
	OH_C	**3600**	**3430**	**170**
SAPO-5	OH_A'	**3630**	**3370**	**260**
	OH_B'	**3513**	-	-

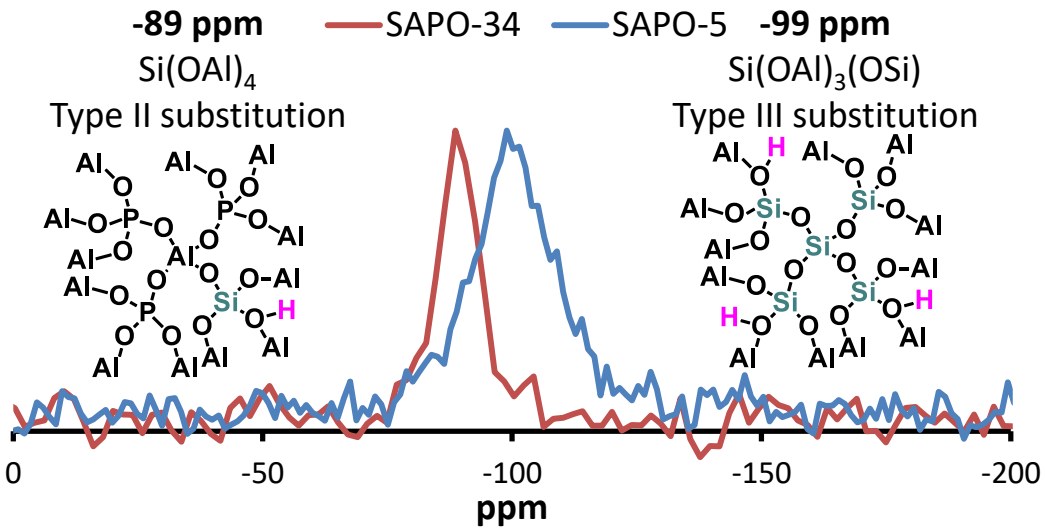

Figure 3 ^{29}Si MAS NMR spectra of SAPO-5(1.38) and SAPO-34(2.66) catalysts obtained at 9.4T using ramped cross polarization at 8 kHz.

The precise nature and behavior of the silicon acid sites was investigated using a combination of ^{29}Si MAS NMR to confirm the location and coordination geometry of the silicon species, and probe-based FTIR spectroscopy (discussed above) was used to rationalize the intrinsic behavior of the catalytically active acid sites. The main peak observed through ^{29}Si NMR for the SAPO-34 catalyst (-89 ppm, Figure 3 & Figure S8) was assigned, based on peak position, as an isolated, acidic $Si(OAl)_4$ site, formed through type II substitution.[41] The SAPO-5 catalyst shows a broad signal spanning a range of -90 to -110 ppm (Figure 3 & Figure S9), this is characteristic of silicon substituting in a range of sites, with varying amounts of aluminum and silicon neighbors. The maximum intensity is at -99 ppm, suggesting the $Si(OSi)(OAl)_3$ environment is dominant.[42] It is to be noted that Si-O-P bonds are not seen in the SAPO cata-lysts.[43] The contrasting silicon incorporation mechanisms between the AlPO-34 and AlPO-5 frameworks suggest that the specific nature of the active site formed is intrinsically dependent on the specific framework host architecture.

On establishing the link between the nature of the active site and specific AlPO frameworks, theoretical methods can be used to further augment the inherent nature of the site-selective frameworks. To ful-

ly understand this phenomenon it is necessary to gain insights on an electronic level using *ab initio* calculations, thereby affording structure-property correlations to be established, which can facilitate the proficient design of tailor-made catalysts for a range of sustainable acid-catalyzed processes.

We have found that despite the energy of forming an isolated silicon site by type II substitution ($\Delta_{Sub,1}$) being congruent in both the SAPO-5 (AFI) and SAPO-34 (CHA) architectures, the preferred orientation of the proton is very different. The SAPO-5 proton species maximizes hydrogen bonding interactions by residing inside the inaccessible 6-membered rings of the microporous architecture. In stark contrast, the proton species in SAPO-34 points into the pore of the three-dimensional channel architecture, and is accessible to both probe molecules and reactants, as substantiated by FTIR results earlier. In light of this, the energy of forming a silicon site through type III substitution ($\Delta_{Sub,2}$) is subtly lower (and therefore more favorable) in the AFI framework when compared to the chabazite SAPO-34 framework (Table 4). It is important to note that such a species ($(PO)_3$-Si-O-Si-$(AlO)_3$) is highly unlikely to form.[11] As type III substitution facilitates the formation of silicon islands and siliceous phases within the SAPO framework, it is highly likely that the CHA structure would enable the generation of isolated sites, whereas the silicon in AFI would tend to cluster. Whilst this form of isolated, strict type III substitution site is unlikely to occur, the more realistic 5-silicon island has been modeled and the calculations confirm that silicon clustering more readily occurs in the SAPO-5 system than the SAPO-34. Given the smaller $\Delta_{Sub,5}$ value of SAPO-5 compared to SAPO-34, as corroborated by the ^{29}Si NMR findings (Figure 1). This is again attributed to the ease with which Si-O-Si bonds can be formed within the AFI architecture, facilitating the formation of silicon islands. However, in the CHA architecture, Si-O-Si bonds are less favored, forcing the formation of isolated silicon and Brønsted acid sites. This finding further reinforces the notion that framework architectures and silicon substitution mechanisms are intrinsically linked.

TABLE 4: Energies of formation of silicon sites in SAPO-34 and SAPO-5 frameworks.

System	*SAPO-5 / eV (Unit Cell)$^{-1}$*	*SAPO-34 / eV (Unit Cell)$^{-1}$*
$\Delta_{Sub,1}$	5.4 ± 0.05	5.4 ± 0.05
$\Delta_{Sub,2}$	8.8 ± 0.05	8.9 ± 0.05
$\Delta_{Sub,5}$	23.6 ± 0.05	24.0 ± 0.05

The specific acid sites observed through ^{29}Si NMR (Si(OAl)4 in SAPO-34, and Si(OSi)4 in SAPO-5) were explored in greater detail through a theoretical probe-based binding study with ammonia and ethanol. It was found that ammonia bound most strongly to the isolated SAPO-34 silicon site, suggesting that the acid sites are stronger than the available protons in the 5-silicon SAPO-5 site. Ethanol was found to behave in an analogous fashion, showing a greater propensity for SAPO-34 (Figure 4) than the SAPO-5 catalyst (Figures S10-S14, Table 5). These observations are concurrent with reported literature findings,[44,45] and further vindicated by our characterization and catalysis results (see below).

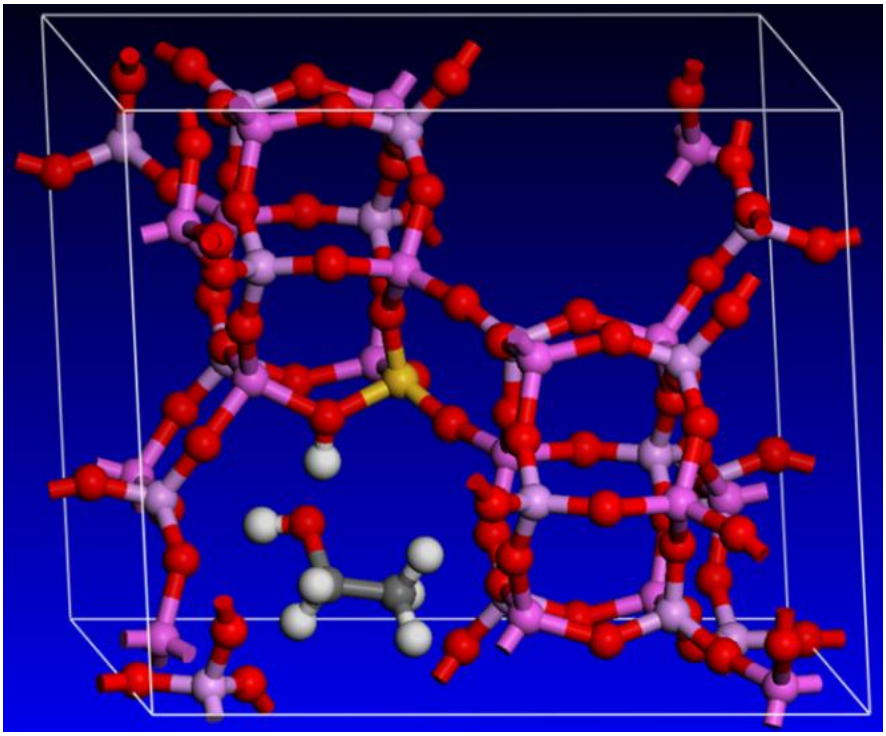

Figure 4 Optimized geometry of the isolated silicon sites in SAPO-34 binding to ethanol.

TABLE 5: Binding energies of silicon sites in SAPO-34 and SAPO-5 frameworks for different probe molecules.

Probe	$\Delta_{Binding}$ / kJ mol^{-1}	
	(5-silicon) *SAPO-5*	*(1-silicon)* *SAPO-34*
Ammonia	-100.2 ± 0.1	-121.9 ±0.1
Ethanol	-73.3 ± 0.1	-89.5 ± 0.1

The variations in both the nature of the acid site and silicon substitution pathways between the SAPO-34 and SAPO-5 frameworks are further accentuated by the contrasting behavior of the two architectures for ethanol dehydration. Whilst all catalysts afforded high conversions over the studied temperature range, distinct differences in selectivity (to ethylene) are apparent. The SAPO-5 catalysts, whilst still active at lower temperatures (conventional heterogeneous catalysts have proved effective only at temperatures >350 °C),[45] begins to favor the production of the diethyl ether by-product at lower temperatures (<300 °C), thereby having a profound influence on the ethylene selectivity, with no other products detected. In stark contrast, both the SAPO-34 catalysts consistently display a strong preference for the formation of ethylene, even at lower temperatures (SAPO-34(2.66) achieves 76 % selectivity at 250 °C, Figure 5, Table S5).

Contrasting the different silicon loadings within the same framework again emphasizes the need to optimize synthetic protocols for adroit catalyst design. The different SAPO-5 frameworks further emphasize and accentuate the importance of site-isolation and the catalytic potential of discrete single-sites. Whilst the SAPO-5(1.80) catalyst (Figure 5A) has a higher amount of silicon than the SAPO-5(1.38) catalyst (Figure 5C), this has not resulted in the generation of a greater fraction acid sites (Figure 1B, Table 2).

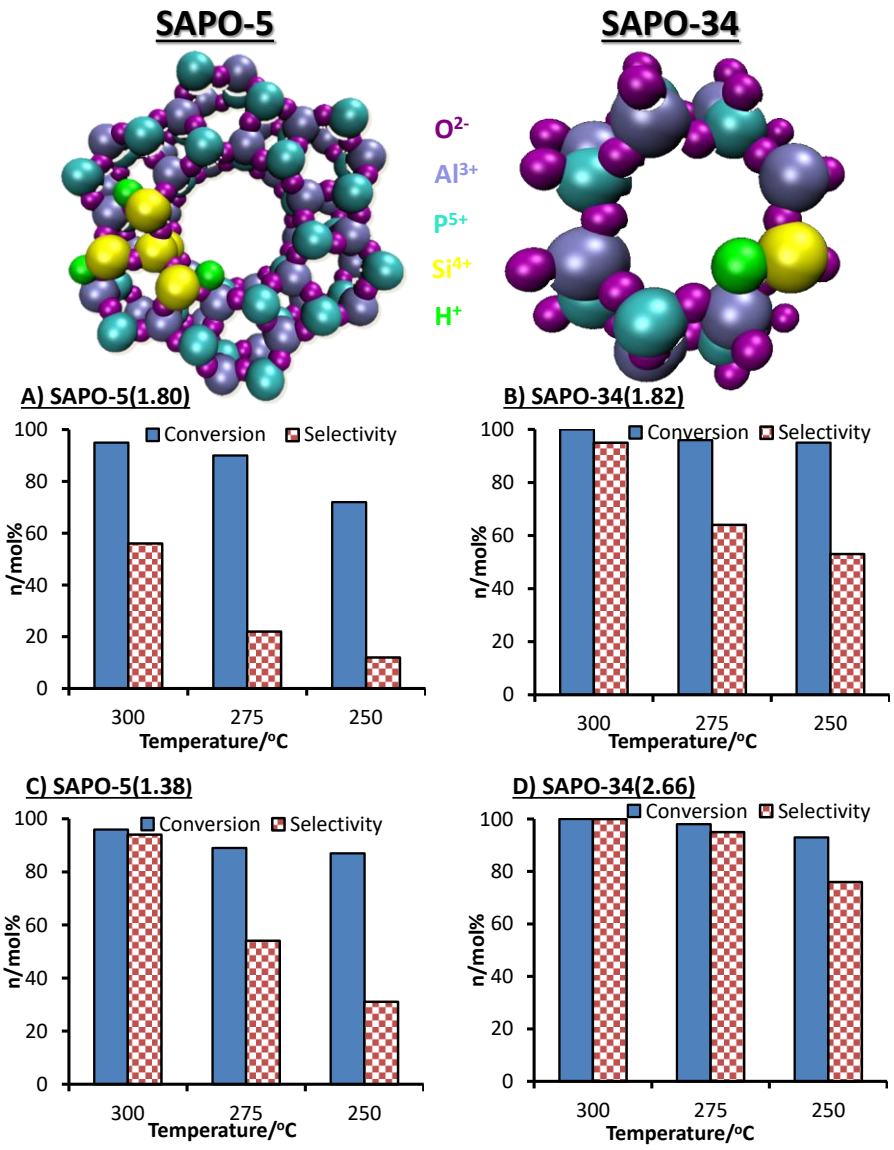

Figure 5 Ethanol conversion and ethylene selectivity observed with SAPO-5 and SAPO-34 frameworks with different silicon content; 0.3 g catalyst, He carrier gas = 50 mL min^{-1}, WHSV = 4.38 h^{-1}. The only other product observed was diethyl ether and mass-balances were close to 99.5%.

The increased silicon loading in the SAPO-5(1.80) has instead facilitated silicon-islanding, through increased type III substitution (Scheme S1), resulting in the formation of siliceous phases, instead of the desired isolated Brønsted acid species. Consequently, this has a marked effect on the catalytic performance of the two materials: the higher loading SAPO-5(1.80) catalyst produces significantly more di-

ethyl ether (rather than ethylene) when compared to the lower loading SAPO-5(1.38) catalyst. The lower silicon loadings, within the SAPO-5 architecture, clearly facilitate the formation of ethylene.

In stark contrast, reducing the silicon loading in the SAPO-34 catalyst has a negative effect on the catalytic performance. The SAPO-34 catalyst effectively facilitates the formation of isolated Brønsted acid centers within the framework, even at higher silicon loadings (Figure 1B, Table 2), leading to the generation of a significant fraction of isolated Brønsted acid sites. By restricting the quantity of silicon dopant, the site-isolation is still maintained, but the total number of Brønsted acid sites is greatly reduced (Figure 1A), which has a marked effect on the catalytic performance of the SAPO-34(1.82) catalyst (Figure 5B) – this phenomenon is particularly accentuated when considering the ethylene selectivity at temperatures < 300 ^{o}C. On the other hand, the SAPO-34(2.66) catalyst (Figure 5D), which despite having a greater quantity of Si active centers, retained its propensity for isolated active sites, thus displaying enhanced conversion and ethylene selectivities, even at temperatures as low as 250^{o}C. Thus the disparate behavior between the two frameworks confirms the delicacy and subtleties involved in achieving optimal catalyst design. While both SAPO-34(1.82) and SAPO-5(1.80) species do also possess phase-impurities (Figure S4) it should be emphasized that such impurities are in very low quantities, however their influence cannot (at this stage) be distinguished from that of the primary phase. The key factor, in both cases, is the (isolated) nature of the active Si center, and not the overall quantity present, that is the crucial determinant in the catalytic activity and selectivity.

By modifying the catalytic conditions (such as the WHSV, see Figure 6) it is possible to further increase the ethylene selectivity (> 90%) when operating at low reaction temperatures (~250 °C), offering potential scope to optimize the production of ethylene at low-temperatures, thereby affording considerable advantages in energy-efficiency from a commercial perspective.[12-14] It should be stressed that when an optimal catalyst is used (SAPO-34(2.66) or SAPO-5(1.38)) then this modification can improve the overall ethylene yield, though this has little effect on non-optimal systems, such as SAPO-34(1.82) and SAPO-5(1.80), which due to their comparatively inferior activity and selectivity (resulting from silicon-islands or lower fraction of acid sites), would not be ideal candidates for full optimization.

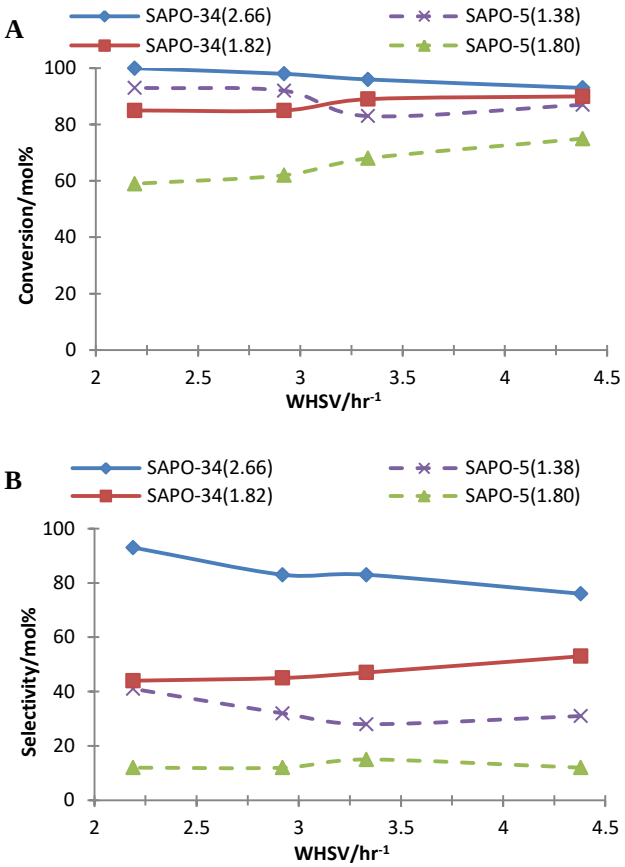

Figure 6 Influence of WHSV on ethanol conversion (A) and ethylene selectivity (B) with SAPO-34 and SAPO-5 catalysts at 250 °C, 0.3 g catalyst, He carrier gas = 50 mL min^{-1}. The only other product observed was diethyl ether and mass-balances were close to 99.5%.

The propensity of the catalysts to selectively produce ethylene from the by-product, diethyl ether, was also investigated (Figure 7). In this example, we wish to particularly highlight the most striking difference between the two frameworks, their reactivity. This observation implies that superior ethylene yields of the SAPO-34 catalysts (when ethanol is employed as a feedstock) derive not from an enhanced ability to activate ethanol, but from the ability to efficiently transform diethyl ether into ethylene, thus lowering the quantity of by-products and improving the overall efficiency of the reaction. Whilst it is evident from Figure 5, that both the SAPO-5 and SAPO-34 frameworks are all capable of activating ethanol to a reasonable degree (high conversions), it is apparent that only the SAPO-34 catalysts effec-

tively catalyze the formation of ethylene (Figure 7), further elucidating the contrasting behavior when diethyl ether and ethanol are used as feedstocks.

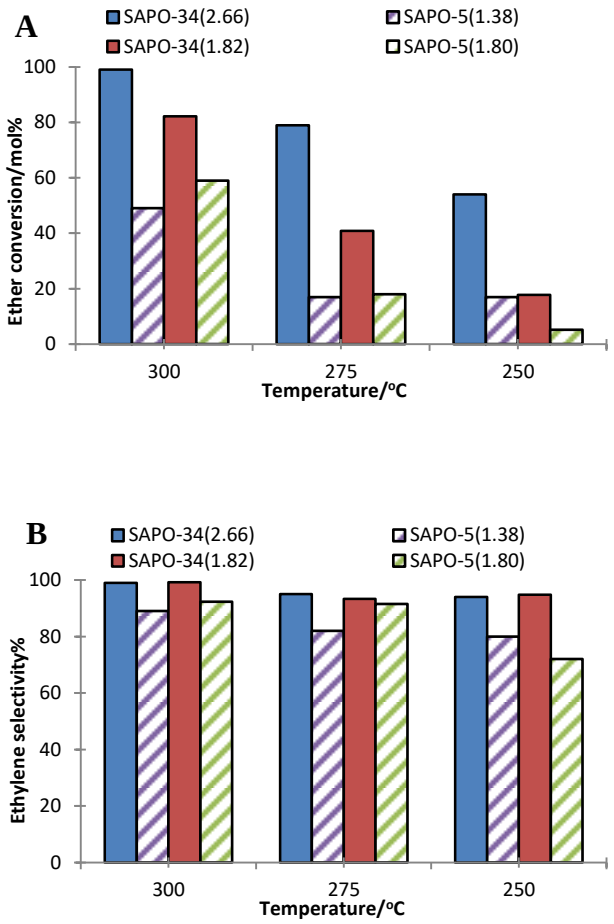

Figure 7 Conversion of diethyl ether (A) and selectivity to ethylene (B) with SAPO-34 and SAPO-5 catalysts, 0.3 g catalyst, He carrier gas = 50 mL min^{-1}, WHSV = 4.38 h^{-1}. The only other product observed was ethanol and mass-balances were close to 99.5%.

The combined ethanol and diethyl ether dehydration studies highlight some interesting mechanistic implications. Dehydration of ethanol to the olefin may be postulated (Scheme 1) to occur via direct dehydration of ethanol to ethylene (intramolecular pathway, Scheme 1A) or involving formation of diethyl ether which can then react further to form ethylene (intermolecular pathway, Scheme 1B & 1C).

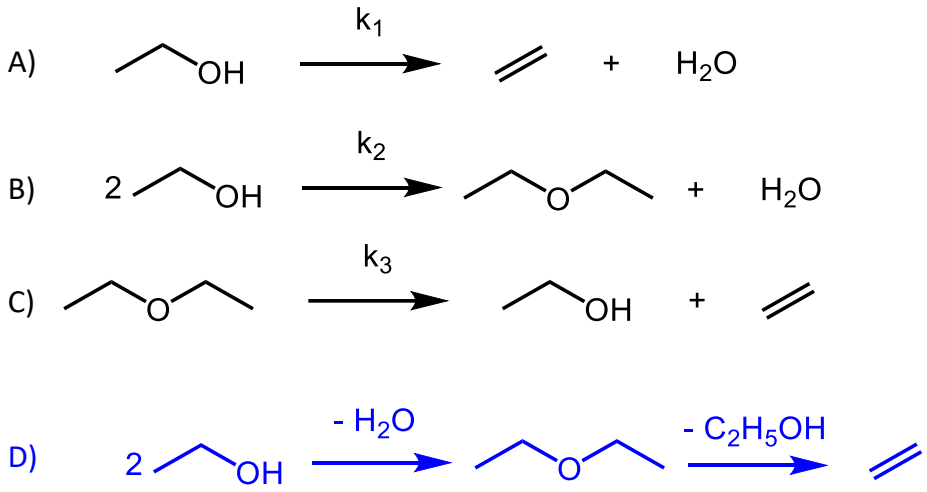

Scheme 1 Three plausible mechanistic pathways (A, B & C) and the suggested mechanistic pathway operating with the SAPO catalysts (D).

The formation and subsequent reactivity of diethyl ether from our studies (Figure 7) suggests the plausibility of Scheme 1C, the dehydration of ether to ethylene either via an S_N2 mechanism with water[46] or an E1 reaction mechanism.[47] To further investigate the mechanistic significance, a preliminary catalytic study was performed using the (most active and selective) SAPO-34(2.66) catalyst, employing both ethanol and diethyl ether as feedstocks (Figure 8). When the reaction was carried out with ethanol as the feedstock at low contact times (fast flow-rates), there is very little ethanol present in the product stream. This suggests that under these conditions the activation of ethanol is not the crucial determinant with the SAPO catalysts; as it can be achieved facilely even at low contact times. However, looking closely at the product composition, it is clear that, at low contact times, diethyl ether is the principal product, with only minor quantities of ethylene being formed. This supports our hypothesis that, ethanol is rapidly converted to diethyl ether in the first step (Scheme 1A), even at low contact times. Ethylene is produced in minor quantities, though at this stage, it is not clear if this is formed from diethyl ether or ethanol. Increasing the contact time has very little effect on the ethanol composition, though interestingly, the yields of diethyl ether and ethylene are now inversely correlated. Given the above and the fact that ethanol primarily forms diethyl ether and not ethylene in the first stage, we can hypothesize that

ethylene is primarily produced from diethyl ether and not ethanol. These results are further vindicated by using diethyl ether as the feedstock (Figure 8B). Similarly there were small quantities of ethanol produced, however the ethylene and diethyl ether compositions are again inversely related. This is again consistent with the more rapid formation of diethyl ether and the slower subsequent dehydration to form ethylene.

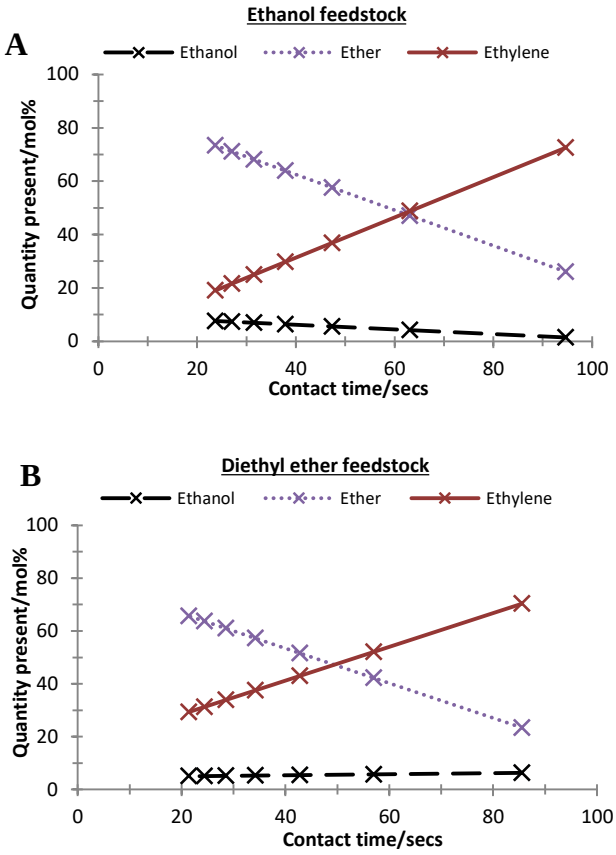

Figure 8 Contrasting the reactivity of the SAPO-34(2.66) catalyst with ethanol (A) and diethyl ether (B) as feedstocks at varying contact times. Conditions: 200°C, Helium flow of 25 mL/min, 0.3 g of catalyst.

From our initial kinetic studies, it is highly likely that the rate of reaction (k2) for pathway B (see Scheme 1)[48] is greater than pathway C (k3). Nevertheless, the experimental evidence does not allow the direct dehydration route (pathway k1) to be discounted. In fact, Phillips and Datta[6] described the dehydration of ethanol leading to the simultaneous formation of diethyl ether and ethylene with H-ZSM-5.[6]

Whilst more detailed mechanistic studies are currently in progress, our preliminary experimental evidence suggests that these catalysts (especially the SAPO-34) are of sufficiently high acid strength to facilitate the formation of ethylene via diethyl ether (Scheme 1). Indeed, the significant differences in ethanol conversion and associated ethylene selectivity with temperature, compared to diethyl ether conversion and associated ethylene selectivity, suggests it is the reactivity of diethyl ether, rather than ethanol, which is a significant factor in achieving high selectivity to ethylene, though a more thorough catalytic investigation is necessary to confirm that this is the case over a wider range of temperatures.

The variation in catalytic activity between the two SAPO frameworks, with various silicon loadings is a direct response facilitated by the two different frameworks and the two distinct catalytic species present therein. Through the combination of NMR, probe-based FTIR and periodic DFT calculations it has been demonstrated that the differences in catalytic activity and selectivity between the two framework architectures are not just limited to size- and orientation of the pore apertures. The comparatively unexplored energetics of active site incorporation confirms that an explicit relationship exists between active sites and associated frameworks. To this extent, it becomes somewhat possible to target the formation of a specific active site by selectively directing the formation a certain framework topology. It is observed that the nature of the silicon substitution in SAPO-34 generates stronger Brønsted acid sites, akin to those observed in analogous chabazitic zeolites. Further similarities between the zeolitic framework and the silicoaluminophosphate are further evidenced by the presence of defect sites; such as silanols in the former[49] and P-OH in the latter,[50] as observed by the probe-based FTIR measurements in this study. The acid sites present in SAPO-34 are highly active for the acid-catalyzed dehydration of ethanol to ethylene and, as such the SAPO-34 catalyst, which exclusively forms isolated silicon sites, is a good candidate for efficiently performing this reaction.

The role of the individual acid site (isolated vs. islands) can also be linked directly to the framework architecture and topology. Through a combination of probe-based FTIR and periodic DFT studies we show that the inaccessible 6-membered rings of the SAPO-5 framework limit the catalytic potential of the material. While such sites are large enough to accommodate protons, even the smallest molecular

probes (such as CO and NO) are unable to access them, thereby lowering the total number of available protons (and acid sites) to perform the catalytic reaction. In contrast, the three-dimensional channel-structure of the SAPO-34 catalyst provides an accessible path to the internal protons, thereby providing a higher fraction of available active sites for the ensuing catalysis. The relatively few accessible acid sites in the SAPO-5 catalyst are shown to have a proclivity primarily for the dehydration of ethanol to the diethyl ether (k2, Scheme 1), but have been found to be less acidic than their counterparts in the SAPO-34 catalyst, which hinders the further conversion of the diethyl ether to ethylene (k3, Scheme 1). On the other hand, the widely accessible strong acid sites in the SAPO-34 catalyst are able to effectively promote the formation of ethylene from the diethyl ether by-product (k3, Scheme 1), thereby increasing the total ethylene yield at temperatures as low as 250 °C. It is a combination of these factors that makes the smaller pore SAPO-34 system a superior catalyst when compared to the larger-pore SAPO-5 catalyst. In light of this, SAPO-34 has emerged as a superior catalyst for the continuous production of ethylene from ethanol and becomes a viable candidate for potential industrial implementation.[12-14]

4. CONCLUSION

Preliminary structure-property correlations originating from this study have proved invaluable in the design of an effective catalyst for the low-temperature dehydration of ethanol, using tailored SAPO architectures. The pronounced effect of the framework topology has been investigated with respect to silicon substitution mechanisms that lead to the creation and modulation of discrete, isolated solid-acid active sites. The predisposition of these designed active sites for influencing intrinsic catalytic outcomes has been probed using a combined ^{29}Si NMR, probe-based FTIR and periodic DFT study, with a view to understanding the mechanistic features in greater detail. The synthetic protocol adopted for the SAPO-34 catalyst was found to promote the formation of accessible, strong Brønsted acid sites, via the creation of isolated silicon species, which were highly selective for the formation of ethylene. The findings from this study have afforded adequate scope for design of more versatile heterogeneous catalysts[51] and their potential exploitation[12-14] in industrially significant, acid-catalyzed transformations.

ACKNOWLEDGMENT

We wish to thank the British-Italian partnership program for funding this research. MC thanks for support the Royal Society University Research Fellowship scheme. MEC is grateful to SiGNa Chemistry for funding, and we are grateful to Compagnia di San Paolo for sponsorship to NIS – Interdepartmental Centre (Torino). We are also grateful to Cambridge Reactor Design (CRD) for their invaluable help in reactor design and configuration. Danni Sun is acknowledged for her contributions to the mechanistic study.

REFERENCES

(1) Morschbacker, A. *Polym. Rev.* **2009**, *49*, 79-84.

(2) Gucbilmez, Y.; Dogu, T.; Balci, S. *Ind. Eng. Chem. Res.* **2006**, *45*, 3496-3502.

(3) Kito-Borsa, T.; Pacas, D. A.; Selim, S.; Cowley, S. W. *Ind. Eng. Chem. Res.* **1998**, *37*, 3366-3374.

(4) Golay, S.; Kiwi-Minsker, L.; Doepper, R.; Renken, A. *Chem. Eng. Sci.* **1999**, *54*, 3593-3598.

(5) Haber, J.; Pamin, K.; Matachowski, L.; Napruszewska, B.; Poltowicz, J. *J. Catal.* **2002**, *207*, 296-306.

(6) Phillips, C. B.; Datta, R. *Ind. Eng. Chem. Res.* **1997**, *36*, 4466-4475.

(7) Flanigen, E. M.; Lok, B. M.; Patton, R. L.; Wilson, S. T. *Pure Appl. Chem.* **1986**, *58*, 1351-1358.

(8) Lok, B. M.; Messina, C. A.; Patton, R. L.; Gajek, R. T.; Cannan, T. R.; Flanigen, E. M. *J. Am. Chem. Soc.* **1984**, *106*, 6092-6093.

(9) Chen, D.; Sharma, S.; Cardona-Martínez, N.; Dumesic, J. A.; Bell, V. A.; Hodge, G. D.; Madon, R. J. *J. Catal.* **1992**, *136*, 392-402.

(10) Chen, N. Y.; Kaeding, W. W.; Dwyer, F. G. *J. Am. Chem. Soc.* **1979**, *101*, 6783-6784.

(11) Vomscheid, R.; Briend, M.; Pletre, M. J.; Man, P. P.; Barthomeuf, D. *J. Phys. Chem.* **1994**, *98*, 9614-9618.

(12) Lefenfeld, M.; Raja, R.; Paterson, A. J.; Potter, M. E. WO Patent, 2010, WO 2010085708.

(13) Lefenfeld, M.; Raja, R.; Paterson, A. J.; Potter, M. E. US Patent, 2014, US 8,759,599 B2.

(14) Lefenfeld, M.; Raja, R.; Paterson, A. J.; Potter, M. E. EU Patent, 2010, EP 2389245-A2.

(15) Hayashi, S.; Hayamizu, K. *Bull. Chem. Soc. Jpn.* **1991**, *64*, 685-687.

(16) van Beek, J. D. *J. Magn. Reson.* **2007**, *187*, 19-26.

(17) Dovesi, R.; Orlando, R.; Civalleri, B.; Roetti, C.; Saunders, V.R.; Zicovich-Wilson, C.M. *Z. Kristallogr.*, **2005**, 220, 571-573.

(18) Becke, A.D. *J. Phys. Chem.*, **1993**, *98*, 5648-5652.

(19) Lee, C.; Yang, W.; Parr, R.G. *Phys. Rev. B*, **1988**, *37*, 785-789.

(20) Vosko, S.H.; Willk, L.; Nusair, M. *Can. J. Phys.*, **1980**, *58*, 1200-1211.

(21) Stephens, P.J.; Devlin, F.J.; Chabalowski, C.F.; Frisch, M.J. *J. Phys. Chem.*, **1994**, 11623-11627.

(22) CRYSTAL Basis Sets Library. (http://www.crystal.unito.it/Basis_Sets/Ptable.html) accessed November 2011.

(23) Sanchez-Sanchez, M.; van Grieken, R.; Serrano, D. P.; Melero, J. A. *J. Mater. Chem.* **2009**, *19*, 6833-6841.

(24) Salmasi, M.; Fatemi, S.; Taheri Najafabadi, A. *J. Ind. Eng. Chem.* **2011**, *17*, 755-761.

(25) Makarova, M. A.; Ojo, A. F.; Karim, K.; Hunger, M.; Dwyer, J. *J. Phys. Chem.* **1994**, *98*, 3619-3623.

(26) Knözinger, H.; Huber, S. *J. Chem. Soc., Faraday Trans.* **1998**, *94*, 2047-2059.

(27) Martins, G. A. V.; Berlier, G.; Coluccia, S.; Pastore, H. O.; Superti, G. B.; Gatti, G.; Marchese, L. *J. Phys. Chem. C,* **2007**, *111*, 330-339.

(28) Smith, L.; Cheetham, A. K.; Marchese, L.; Thomas, J. M.; Wright, P. A.; Chen, J.; Gianotti, E. *Catal. Lett.* **1996**, *41*, 13-16.

(29) Bordiga, S.; Regli, L.; Lamberti, C.; Zecchina, A.; Jorgen, M.; Lillerud, K. P. *J. Phys. Chem. B* **2005**, *109*, 7724-7732.

(30) Martins, G. V. A.; Berlier, G.; Bisio, C.; Coluccia, S.; Pastore, H. O.; Marchese, L. *J. Phys. Chem. C* **2008**, *112*, 7193-7200.

(31) Bordiga, S.; Regli, L.; Cocina, D.; Lamberti, C.; Bjorgen, M.; Lillerud, K. P. *J. Phys. Chem. B* **2005**, *109*, 2779-2784.

(32) Smith, L.; Cheetham, A. K.; Morris, R. E.; Marchese, L.; Thomas,J. M.; Wright, P. A.; Chen, J. *Science* **1996**, *271*, 799-802.

(33) Zubkov, S. A.; Kustov, L. M.; Kazansky, V. B.; Girnus, I.; Fricke, R. *J. Chem. Soc.*, *Faraday Trans.* **1991**, *87*, 897-900.

(34) Sastre, G.; Lewis, D. W. *J. Chem. Soc., Faraday Trans*. **1998**, *94*, 3049-3058.

(35) Chen, J.; Wright, P. A.; Natarajan, S.; Thomas, J. M. *Stud. Surf. Sci. Catal*. **1994**, *84*, 1731-1738.

(36) Lee, S. I.; Chon, H. *J. Chem. Soc., Faraday Trans*., **1997**, *93*, 1855-1860.

(37) Müller, G.; Bodis, J.; Eder-Mirth, G.; Kornatowski, J.; Lercher, J. A. *J. Mol. Struct.*, **1997**, *410-411*, 173-178.

(38) Gianotti, E.; Dellarocca, V.; Oliveira, E.C.; Coluccia, S.; Pastore, H.O.; Marchese, L. *Stud. Surf. Sci. Catal*., **2002**, *142*, 1419-1426.

(39) Potter, M. E.; Sun, D.; Gianotti, E.; Manzoli, M.; Raja. R. *Phys. Chem. Chem. Phys.*, **2013**, *15*, 13288-13295.

(40) Gianotti, E.; Manzoli, M.; Potter, M. E.; Shetti, V. N.; Sun, D.; Paterson, J.; Mezza, T. M.; Levy, A.; Raja, R. *Chem. Sci.*, **2014**, *5*, 1810-1819.

(41) Prakash, A. M.; Unnikrishnan, S., *J. Chem. Soc., Faraday Trans.* **1994**, *90, 2291-2296.*

(42) Ashtekar, S.; Chilukuri, S. V. V.; Chackrabarty, D. K., *J. Phys. Chem.* **1994**, *98*, 4878-4883.

(43) Ashtekar, S.; Satyanarayana, C. V. V.; Chakrabarty, D. K. *Proc. Indian Acad. Sci.-Chem. Sci.* **1994**, *106*, 621-628.

(44) Elanany, M.; Vercauteren, D. P.; Kubo, M.; Miyamoto, M. *J. Mol. Catal. A: Chem.*, **2006**, *248*, 181-184.

(45) Campelo, J. M.; Lafont, F.; Marinas, J. M.; Ojeda, M. *Appl. Catal. A*, **2000**, *192*, 85-96.

(46) Xu, X.; C. P. de Almedia, Antal Jr. M. J. *Ind. Eng. Chem. Res.* **1991**, *30*, 1478-1485.

(47) Zhang, M.; Yu, Y. *Ind. Eng. Chem. Res.*, **2013**, *52*, 9505-9514.

(48) Chiang, H.; Bhan, A. *J. Catal.*, **2010**, *271*, 251-261.

(49) Lo, C.; Trout, B. L. *J. Catal.* **2004**, *227*, 77-89.

(50) Marchese, L.; Chen, J.; Thomas, J. M.; Coluccia, S.; Zecchina, A. *J. Phys. Chem.*, **1994**, *98*, 13350-13356.

(51) Raja, R.; Potter, M. E.; Newland, S. H. *Chem. Commun.*, **2014**, *50*, 5940-5957.

SUPPORTING INFORMATION

The Role of Isolated Acid Sites and Influence of Pore Diameter in the Low-Temperature Dehydration of Ethanol

Matthew E. Potter,[†]* Mary E. Cholerton,[†] Julija Kezina,[†] Richard Bounds,[†] Marina Carravetta,[†] Maela Manzoli,[‡] Enrica Gianotti,[ζ] Michael Lefenfeld,[ϕ] and Robert Raja[†]*

[†]School of Chemistry, University of Southampton, University Road, Southampton, SO17 1BJ, United Kingdom
[‡]Department of Chemistry & NIS-Interdepartmental Centre, University of Turin, Via P. Guiria, 10125, Torino, Italy
[ζ]Dipartimento di Scienze e Innovazione Tecnologica, Centro Interdisciplinare Nano-SiSTeMI, Università del Piemonte Orientale, Via T. Michel 11, 15100, Alessandria, Italy
[ϕ]SiGNa Chemistry Inc, 845 Third Avenue, Suite 623, New York City, New York 10022, United States

Corresponding authors Email: M.E.Potter@soton.ac.uk, R.Raja@soton.ac.uk

Contents

Experimental details	Page S2
Catalysis synthesis	Page S2
Characterisation	Page S2
Catalysis	Page S2
Silicon substitution mechanisms	Page S3
Textural characterisation results	Page S3
Powder X-ray diffraction	Page S3
BET surface area measurements	Page S5
Particle size calculations	Page S5
Scanning Electron Microscopy images	Page S6
Probe-based FTIR spectroscopy	Page S7
NMR spectra	Page S8
Computational analysis	Page S9
Additional catalytic data	Page S12
Mechanistic pathways	Page S12
References	Page S12

Experimental details

Catalysis synthesis

The SAPO-34 and SAPO-5 synthesis were prepared according to references 1-3. Key ingredients and synthetic conditions are listed below in Table S1.

In both cases the as-prepared samples were calcined in a tube furnace under a flow of air at 575 ^{o}C for 16 hours yielding a white solid.

	SAPO-5	SAPO-34
Aluminium source	Aluminium hydroxide hydrate (Aldrich)	Aluminium isopropoxide (Aldrich)
Silicon source	Silica sol (40 wt% in H_2O, Aldrich)	Fumed silica (Aldrich)
Structure directing agent	Triethylamine (Fisher)	Tetraethylammonium hydroxide (35 wt% in H_2O, Aldrich)
Crystallization temperature/ °C	180	200
Crystallization time/ h	24	60

Table S1: Summary of synthetic conditions.

Characterisation

ICP-OES measurements were performed by Medac.

Phase purity and crystallinity of materials was confirmed by powder X-ray diffraction. Powder X-ray diffraction (PXD) was carried out using a Bruker D2 Phaser diffractometer using Cu $K_{\alpha1}/K_{\alpha2}$ radiation λ = 1.5418 Å, PXD patterns were run over a 2θ rage of 5-45° with a scan speed of 3° min^{-1} and increment of 0.01°.

Scanning electron microscopy was carried out using a Jeol JSM-5910.

Catalysis

Catalysis was performed using a custom build flow reactor provided by Cambridge Reactor Design. The reactor comprised of a syringe pump, laptop computer, two mass flow controllers, reactor with heater and control box. A 224 mm quartz reactor tube (4 mm id, 6 mm od) with a 4 mm high frit 80 mm from the base of the tube and a gas inlet 25.8 mm from the top was placed inside the heater jacket. Liquid and gas flows were controlled using a Harvard Apparatus Model 33 MA1-55-3333 syringe pump and Brooks IOM585OS mass flow controller respectively and flow rates were input via computer interface.

Silicon substitution mechanisms

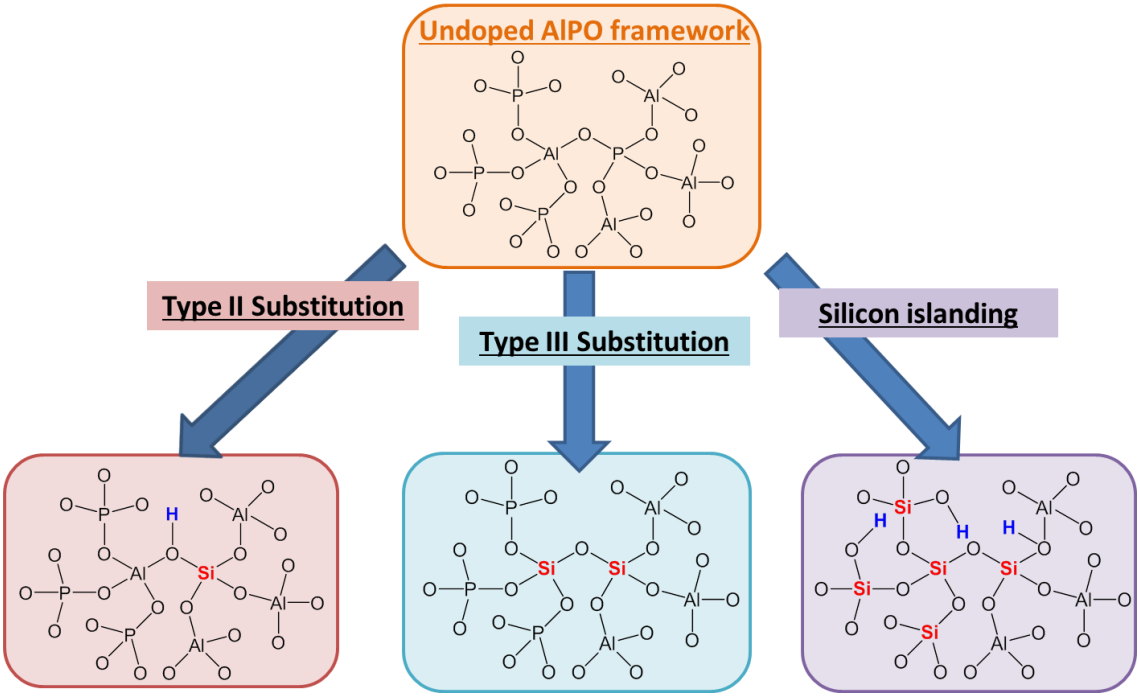

Figure S1: Possible silicon substitution methods into an AlPO framework.

Textural characterization results

Powder X-ray diffraction

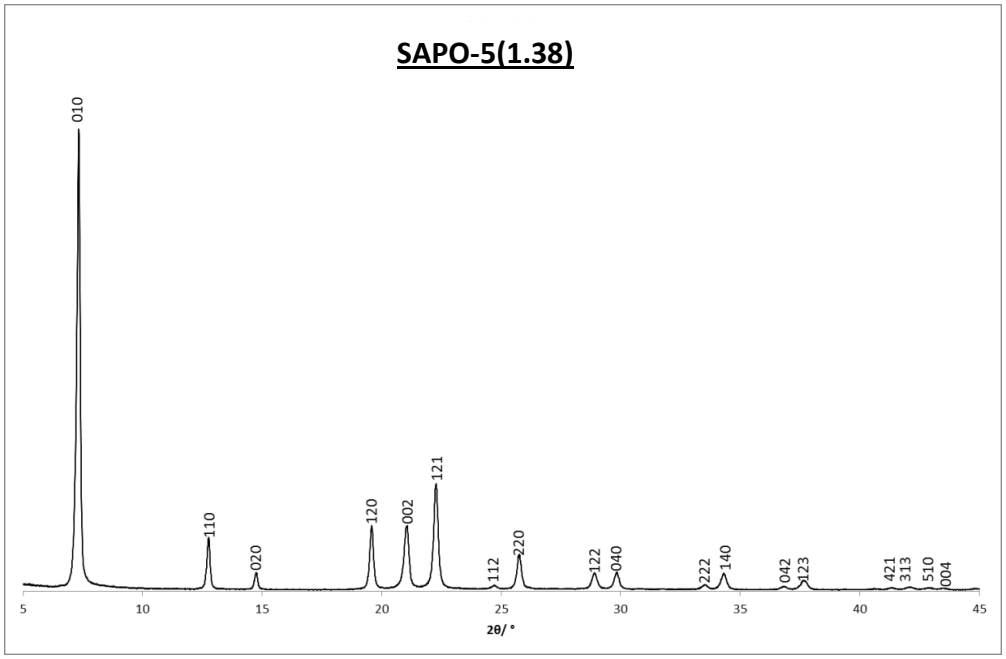

Figure S2: Powder X-ray diffraction pattern for phase-pure SAPO-5(1.38).

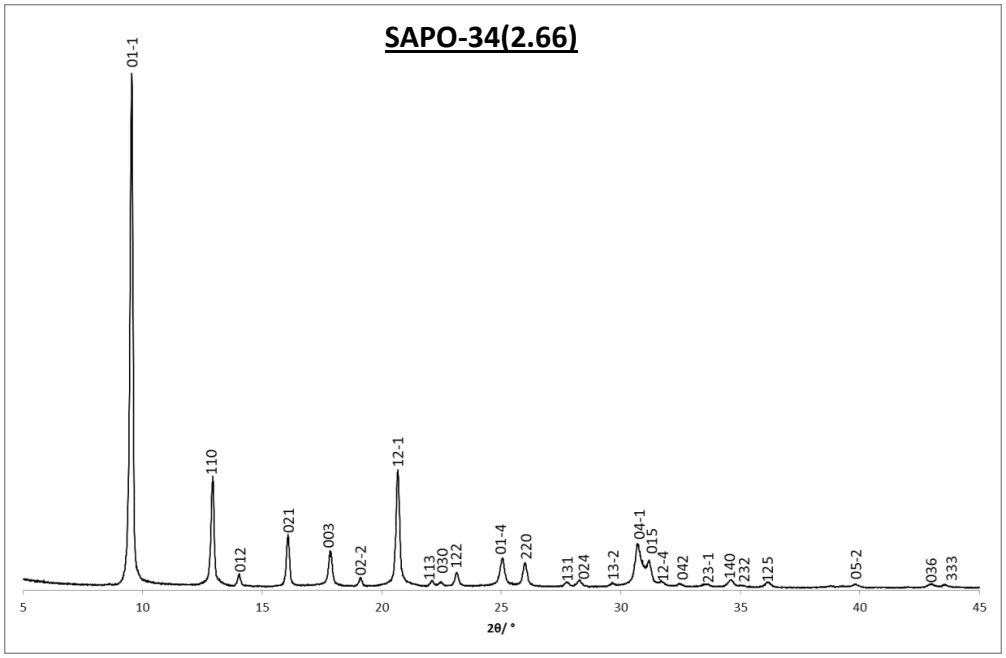

Figure S3: Powder X-ray diffraction pattern for phase-pure SAPO-34(2.66).

Catalyst	Alpha/ Å	Gamma/ Å	Volume/ Å^3
SAPO-5(1.38)	13.8431	8.4295	1398.93
SAPO-34(2.66)	13.7097	14.9052	2426.20

Table S2: Unit cell data for SAPO-5 and SAPO-34 as determined using Celref.[4]

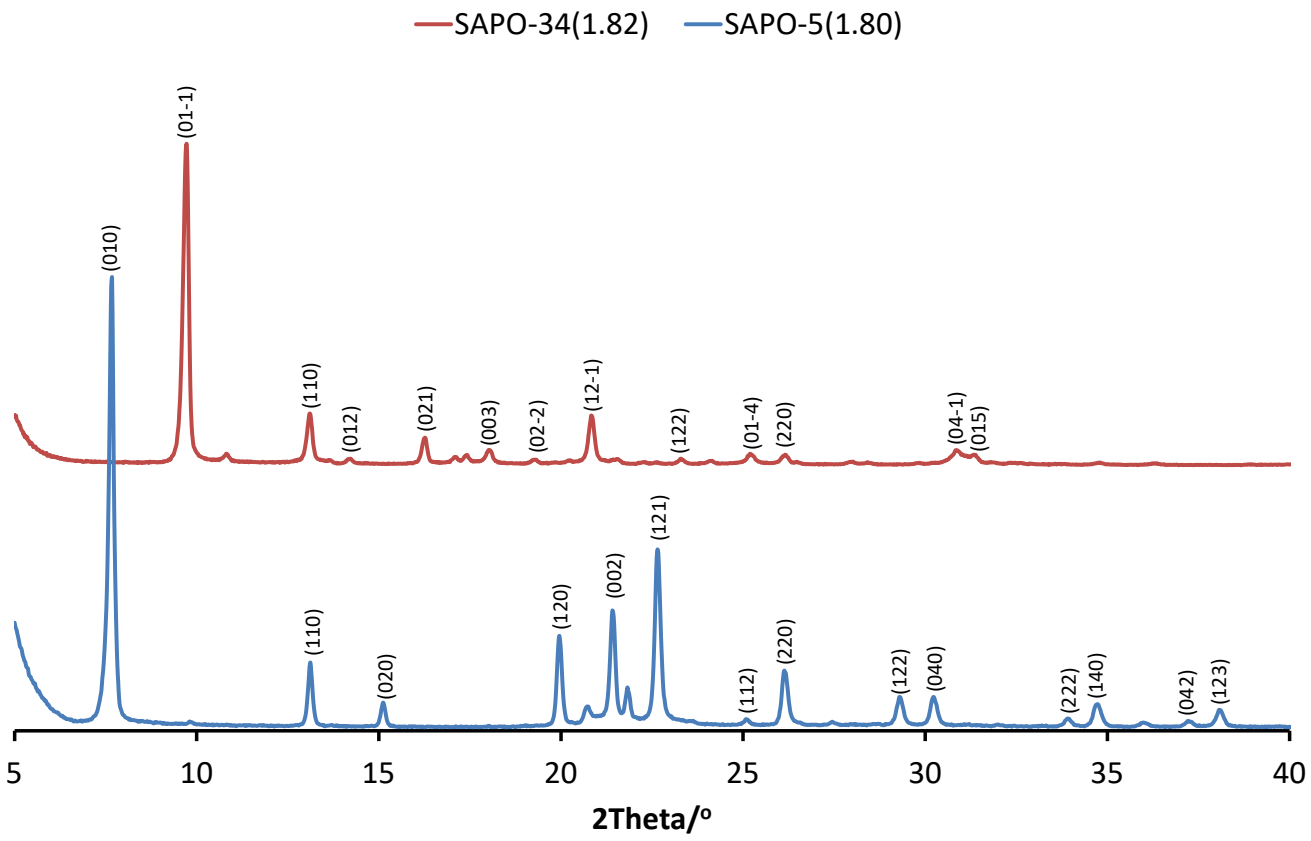

Figure S4: Powder XRD patterns for SAPO-34(1.82) and SAPO-5(1.80) showing main phase.

BET surface area measurements

	SAPO-5(1.38)	SAPO-34(2.66)
BET surface area/ m^2g^{-1}	250.98	479.37

Table S3: Surface area measurements determined using BET.

Particle size calculations

	SAPO-34(2.66)	SAPO-34(1.82)	SAPO-5(1.80)	SAPO-5(1.38)
Particle Size/nm	58	43	59	50

Table S4: Particle sizes derived from powder-XRD with Scherrer's equation.

Scanning Electron Microscopy

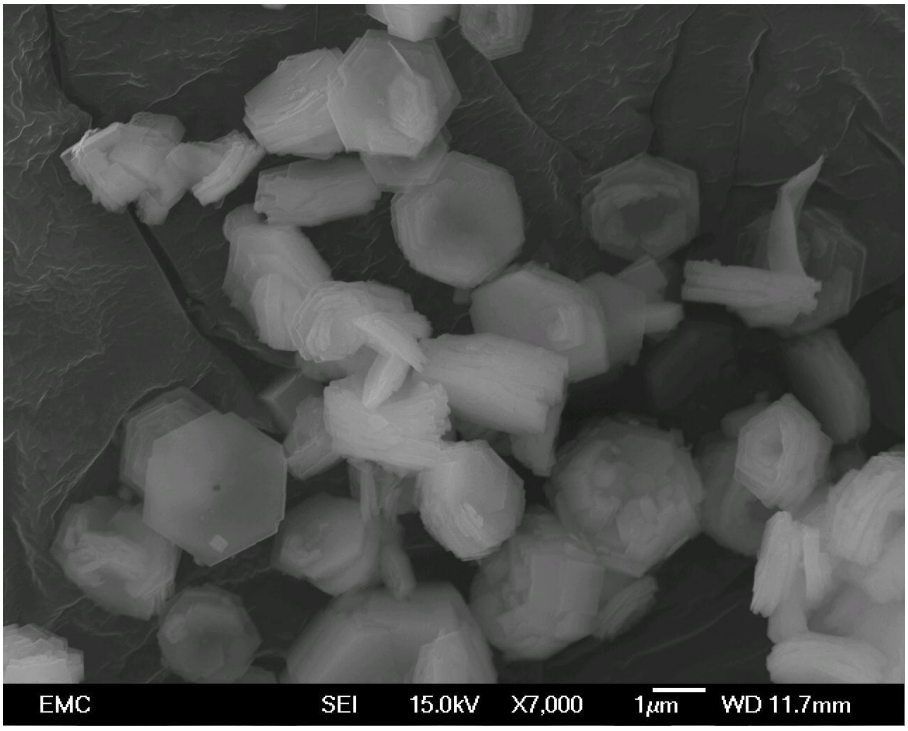

Figure S5: SEM image of SAPO-5(1.38).

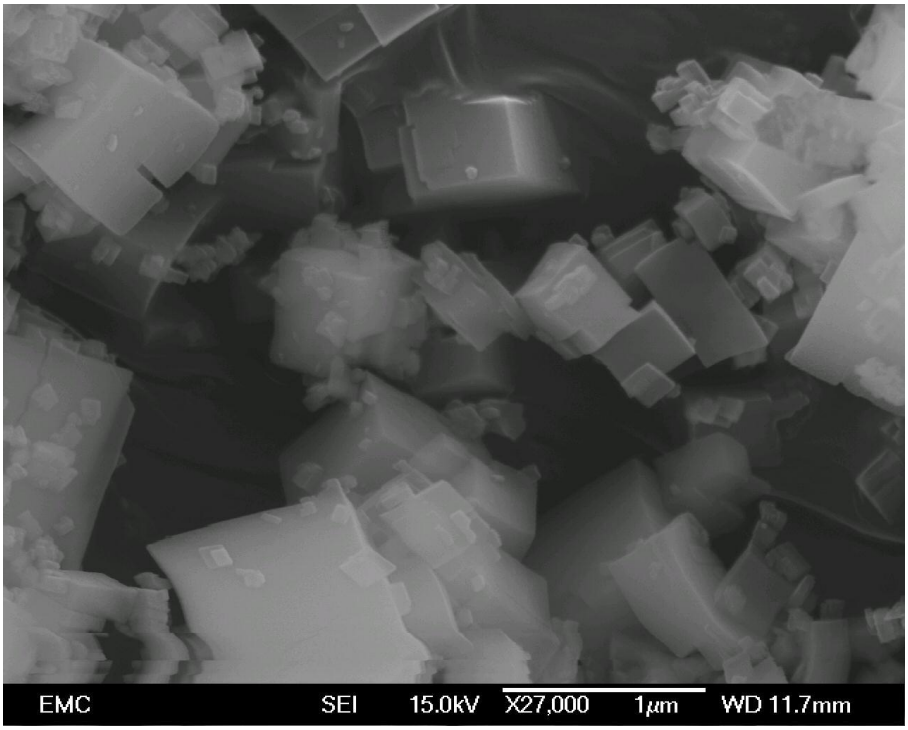

Figure S6: SEM of SAPO-34(2.66).

Probe-based FTIR spectroscopy

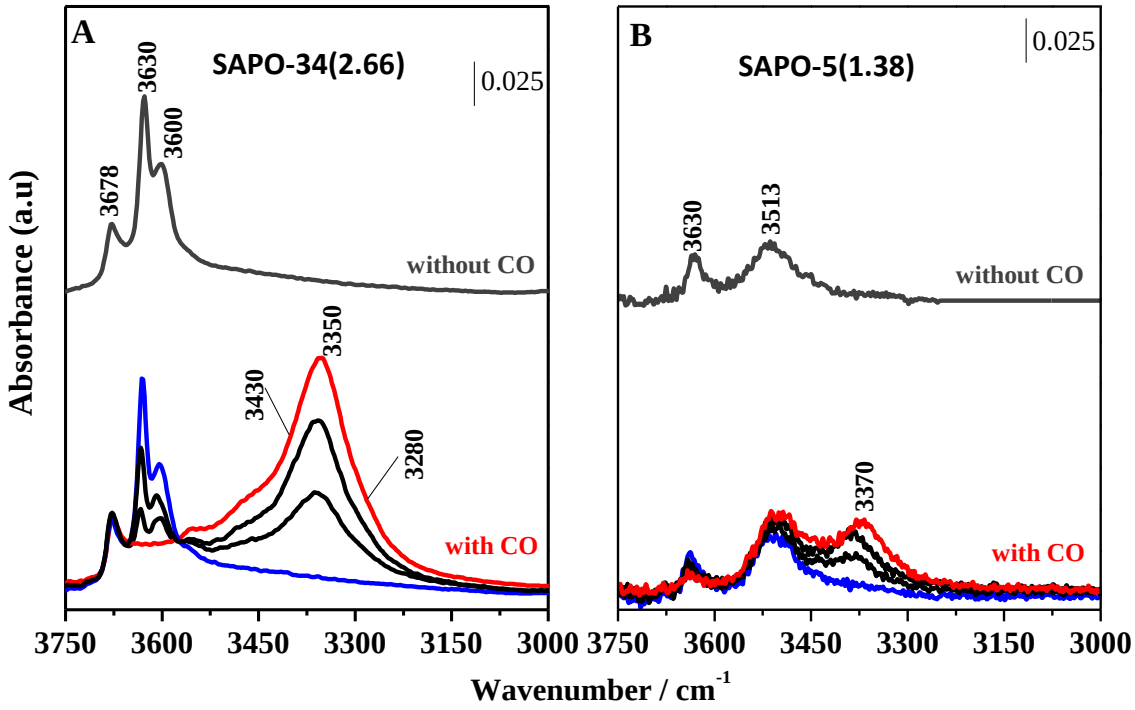

Figure S7: FTIR spectra in the OH stretching region of CO adsorbed at 80 K on calcined SAPO-34(2.66) (A) and SAPO-5(1.38) (B). Decreasing CO coverages from 30 (red curves) to 0.01 (blue curves) mbar. The spectra in vacuo before CO adsorption are also reported (grey curves).

NMR spectra

^{29}Si MAS NMR of SAPO-34(2.66)

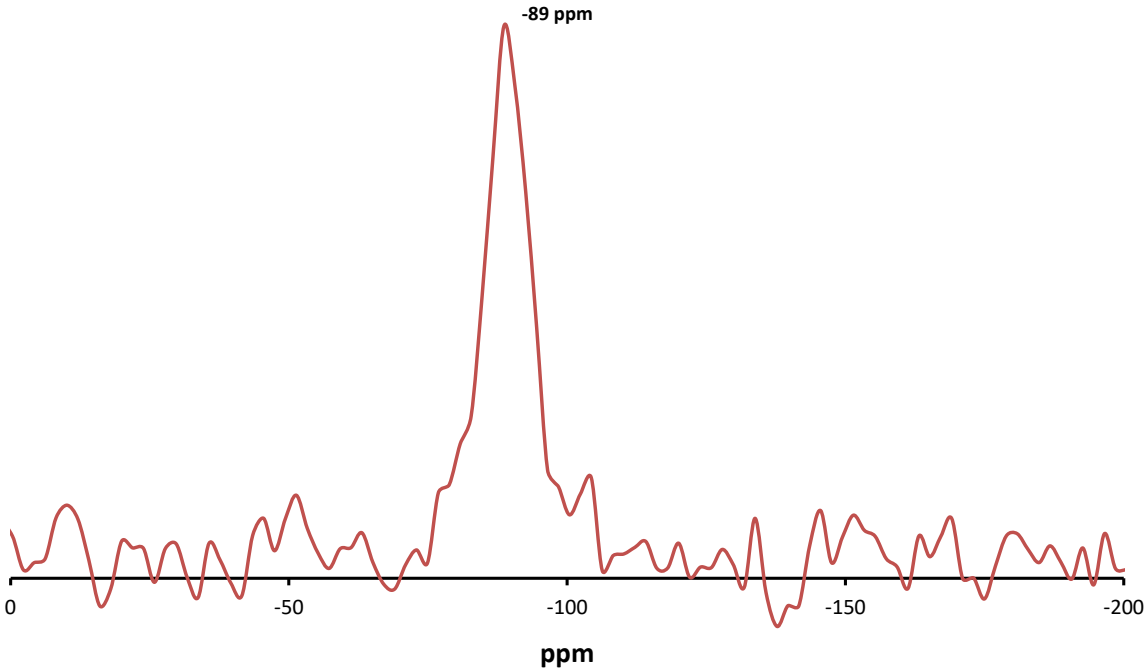

Figure S8: CP-RAMP ^{29}Si MAS NMR spectra of SAPO-34(2.66) at 9.4 T, 8 kHz spin rate. The spectrum is the result of 15000 scans.

^{29}Si MAS NMR of SAPO-5(1.38)

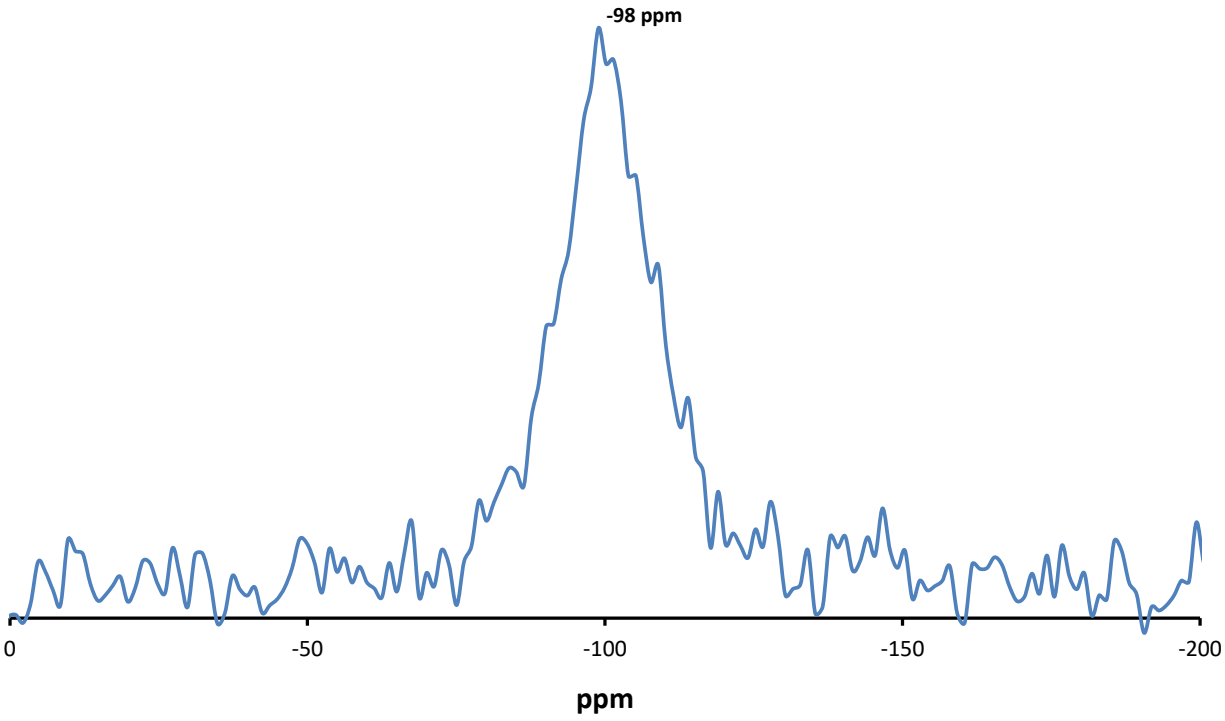

Figure S9: CP-RAMP ^{29}Si MAS NMR spectra of SAPO-5(1.38) at 9.4 T, 8 kHz spin rate. The spectrum is the result of 25000 scans.

Computational Analysis

Binding studies were also performed with NH_3 and ethanol on the specific sites witnessed by ^{29}Si NMR, to gain an insight into the acidic nature of the specific active sites and the mechanistic implications; the following equation was used to quantify the degree of interaction with the probe molecules:

(4) $\Delta_{Binding}$ = E[Probe + SAPO] – E[Probe] – E[SAPO]

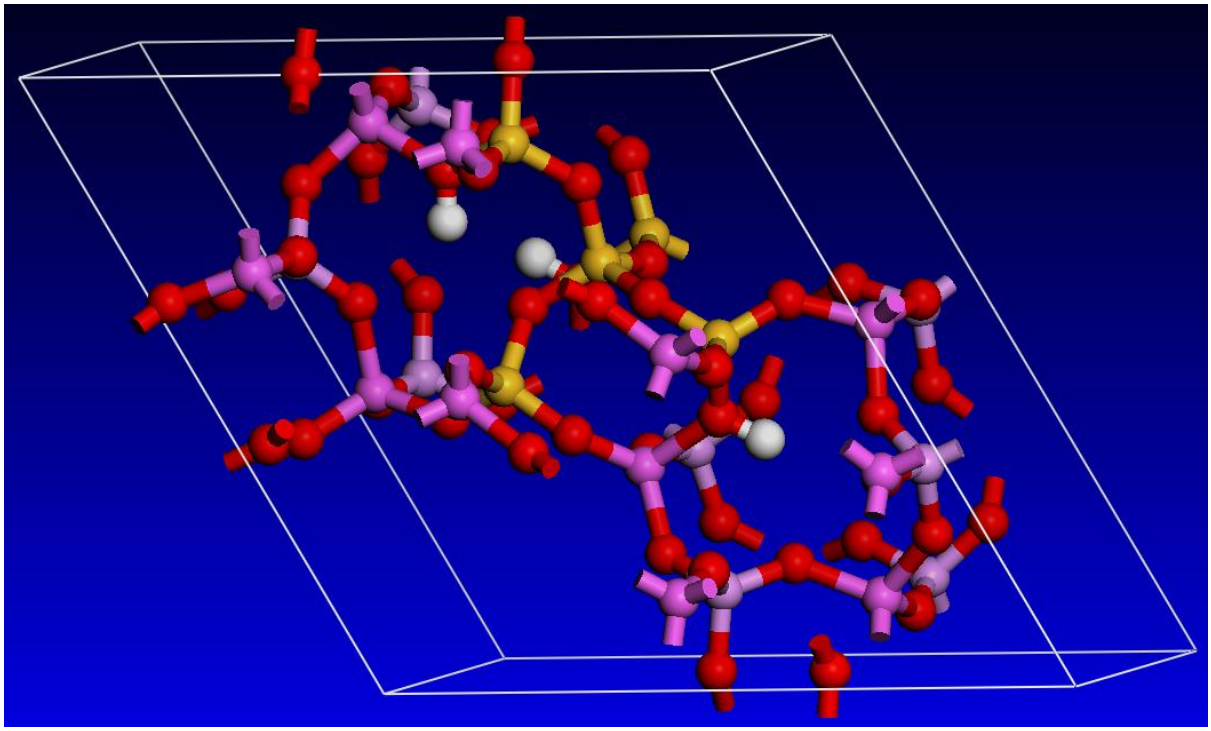

Figure S10: Optimised geometry of the 5-silicon island in SAPO-5.

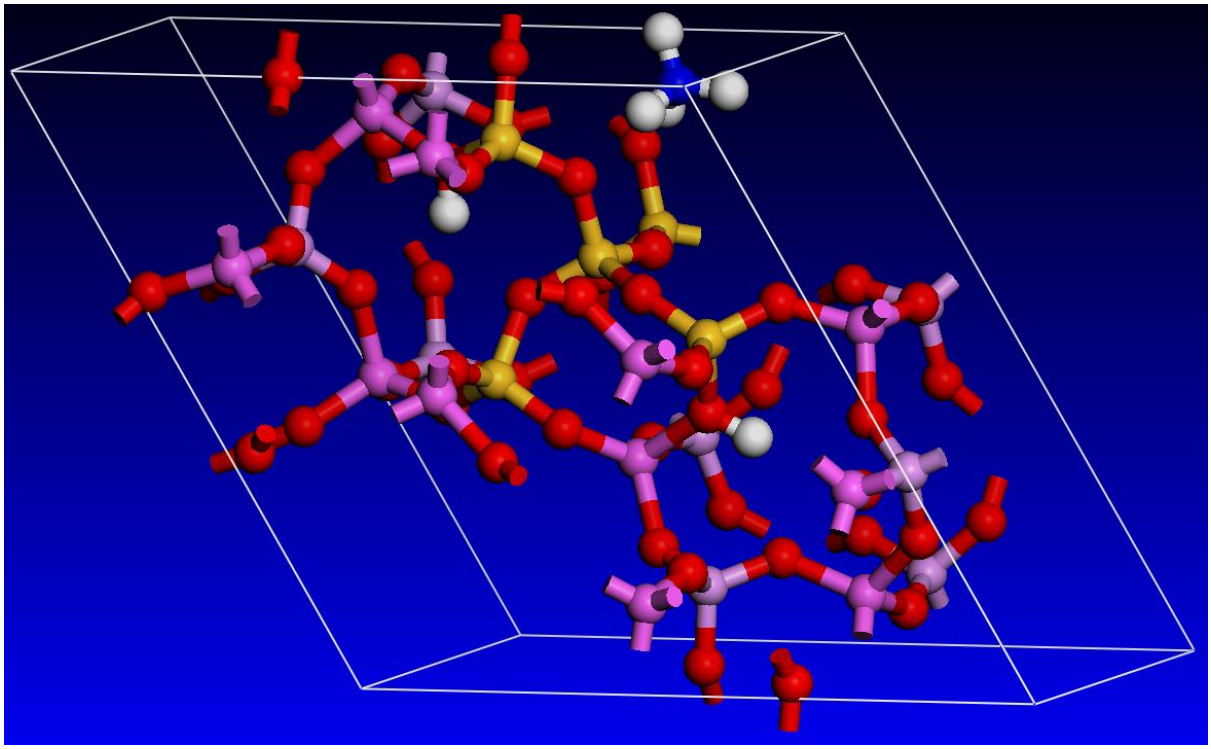

Figure S11: Optimised geometry of the binding of NH_3 to the 5-silicon SAPO-5 species.

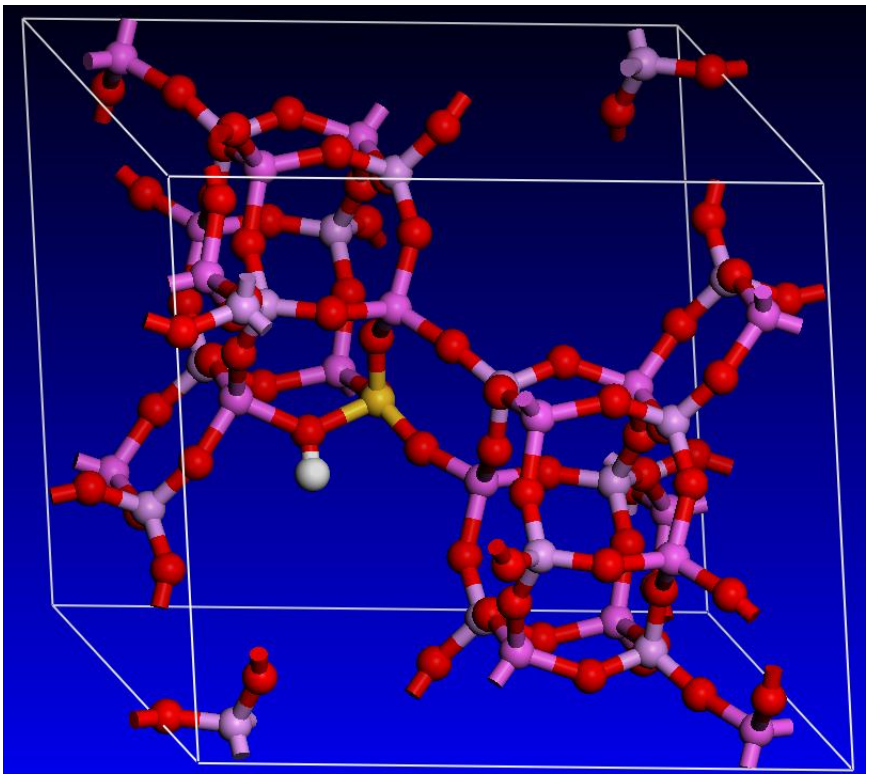

Figure S12: Optimised geometry of the isolated silicon site in SAPO-34.

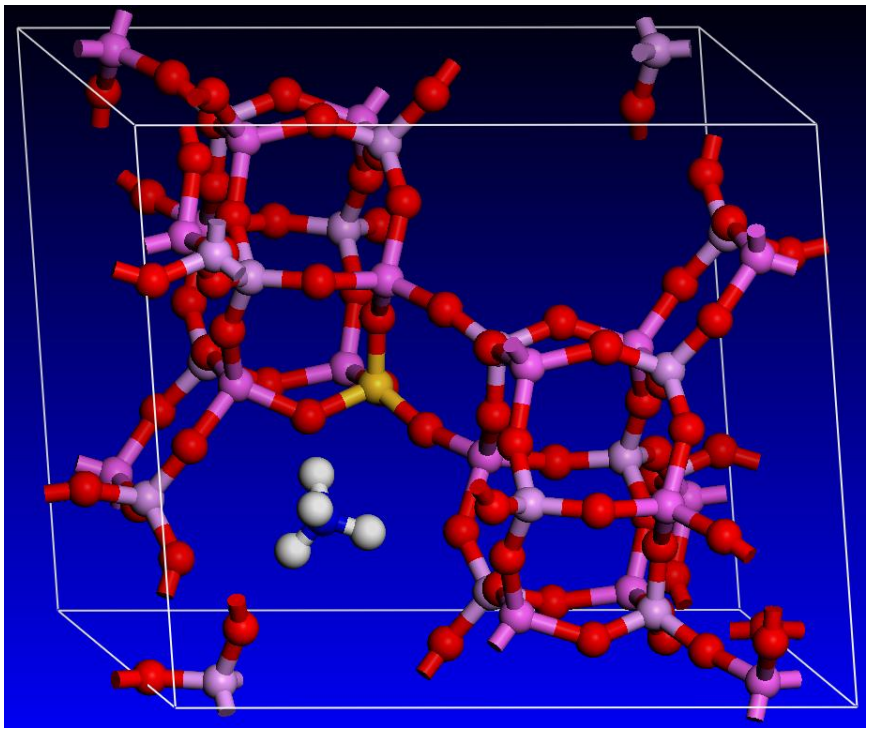

Figure S13: The optimised geometry of the isolated silicon site in SAPO-34 binding to NH_3.

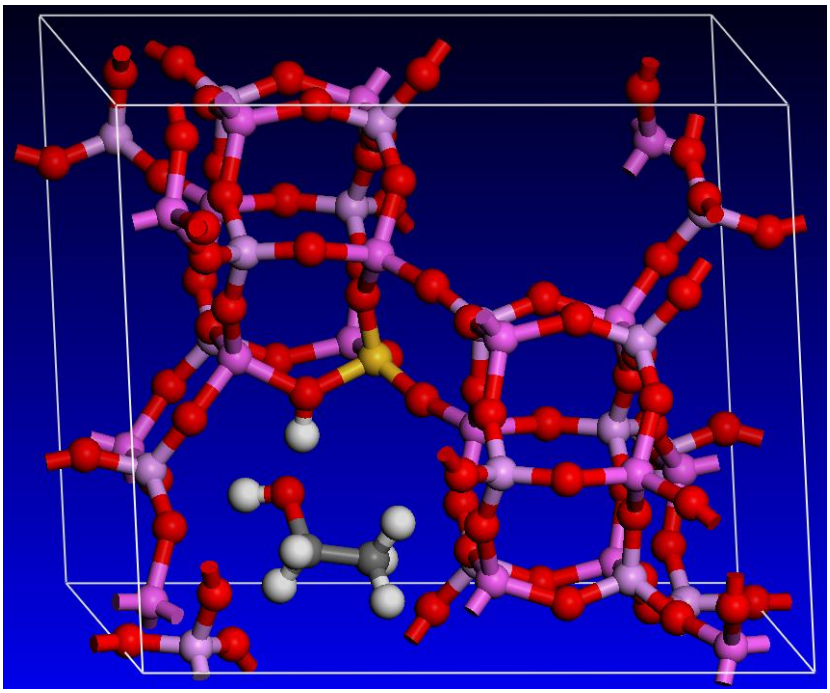

Figure S14: The optimised geometry of the isolated silicon site in SAPO-34 binding to ethanol.

Additional catalytic data

Catalyst	Conversion/mol%			Selectivity/mol%		
	300 °C	275 °C	250 °C	300 °C	275 °C	250 °C
SAPO-5(1.38)	96	89	87	94	54	31
SAPO-34(2.66)	100	98	93	100	95	76
Blank (No catalyst)	0.3	0.3	0.3	20.8	25.3	0.0

Table S5: Catalytic data for dehydration of ethanol to ethylene. WHSV = 4.38 h^{-1}, He carrier gas 50 mL min^{-1}, 0.3 g catalyst. Blank reaction performed using comparable flow rates.

References

[1] Lefenfeld, M.; Raja, R.; Paterson, A. J.; Potter, M. E. WO Patent, 2010, WO/2010085708.

[2] Lefenfeld, M.; Raja, R.; Paterson, A. J.; Potter, M. E. US Patent, 2014, US 8,759,599 B2.

[3] Lefenfeld, M.; Raja, R.; Paterson, A. J.; Potter, M. E. EU Patent, 2010, EP2389245-A2.

[4] Celref, version 3; LMGP (Laboratoire des Materiaux et du Génie Physique de l'Ecole Supérieure de Physique de Grenoble) Suite for Windows: Grenoble, 2000.